Cell

Vertebrate centromeres in mitosis are functionally bipartite structures stabilized by cohesin

Graphical abstract

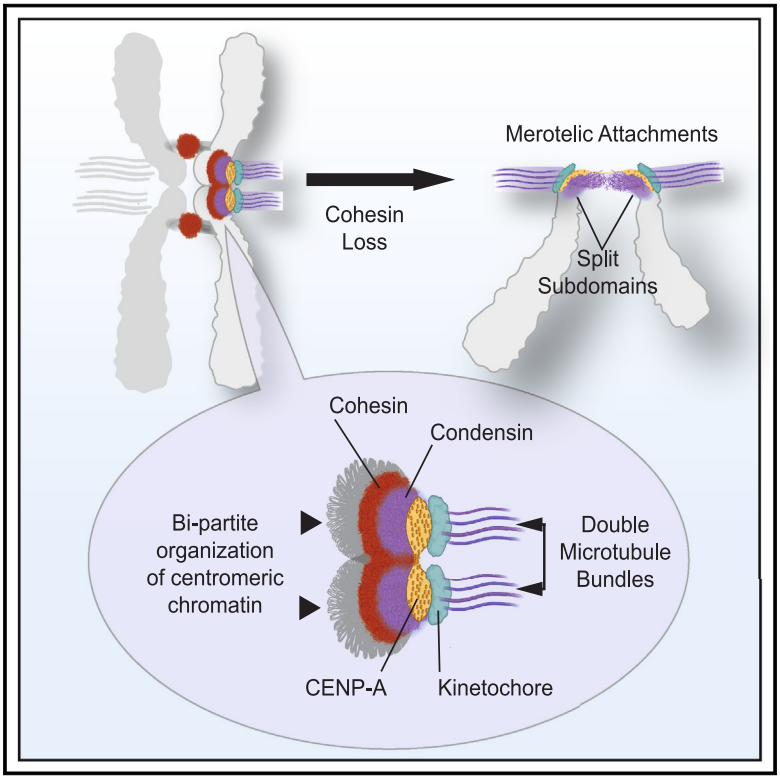

Highlights

- Core centromere chromatin reorganizes into a two-domain structure in mitosis
- Each centromere subdomain engages a discrete microtubule bundle
- Lagging chromosomes in cancer cells have subdomains bound to opposite spindle poles
- Cohesin stabilizes centromere subdomains to avoid formation of merotelic attachments

Authors

Carlos Sacristan, Kumiko Samejima, Lorena Andrade Ruiz, ..., Davide Marenduzzo, William C. Earnshaw, Geert J.P.L. Kops

Correspondence

c.sacristan@hubrecht.eu (C.S.), kumiko.samejima@ed.ac.uk (K.S.), bill.earnshaw@ed.ac.uk (W.C.E.), g.kops@hubrecht.eu (G.J.P.L.K.)

In brief

Sacristan, Samejima et al. report that centromeric chromatin rearranges into a bipartite structure during mitosis, defining two microtubule-binding subdomains on the kinetochore. The engagement of subdomains from single kinetochores to opposite spindle poles is a common configuration of merotelic attachments and a source of chromosomal instability in cancer cells.

Sacristan et al., 2024, Cell *187*, 1–18
June 6, 2024
https://doi.org/10.1016/j.cell.2024.04.014

CellPress

Please cite this article in press as: Sacristan et al., Vertebrate centromeres in mitosis are functionally bipartite structures stabilized by cohesin, Cell (2024), https://doi.org/10.1016/j.cell.2024.04.014

Cell

CellPress
OPEN ACCESS

Article

Vertebrate centromeres in mitosis are functionally bipartite structures stabilized by cohesin

Carlos Sacristan,[1,10,*] Kumiko Samejima,[2,10,*] Lorena Andrade Ruiz,[1] Moonmoon Deb,[2] Maaike L.A. Lambers,[1] Adam Buckle,[3] Chris A. Brackley,[4] Daniel Robertson,[2] Tetsuya Hori,[5] Shaun Webb,[2] Robert Kiewisz,[6,7] Tristan Bepler,[6] Eloïse van Kwawegen,[1] Patrik Risteski,[8] Kruno Vukušić,[8] Iva M. Tolić,[8] Thomas Müller-Reichert,[9] Tatsuo Fukagawa,[5] Nick Gilbert,[3] Davide Marenduzzo,[4] William C. Earnshaw,[2,*] and Geert J.P.L. Kops[1,11,*]

[1]Oncode Institute, Hubrecht Institute, Royal Netherlands Academy of Arts and Sciences (KNAW), and University Medical Center Utrecht, Utrecht, the Netherlands
[2]Wellcome Centre for Cell Biology, Institute of Cell Biology, University of Edinburgh, Edinburgh, UK
[3]MRC Human Genetics Unit, Institute of Genetics & Molecular Medicine, University of Edinburgh, Edinburgh, UK
[4]SUPA School of Physics and Astronomy, University of Edinburgh, Edinburgh, UK
[5]Laboratory of Chromosome Biology, Graduate School of Frontier Biosciences, Osaka University, Suita, Osaka, Japan
[6]Simons Machine Learning Center, New York Structural Biology Center, New York, NY 10027, USA
[7]Biocomputing Unit, Centro Nacional de Biotecnologia (CNB-CSIC), Darwin, 3, Campus Universidad Autonoma, Cantoblanco, Madrid 28049, Spain
[8]Ruđer Bošković Institute, Zagreb, Croatia
[9]Experimental Center, Faculty of Medicine Carl Gustav Carus, Technische Universität Dresden, Dresden, Germany
[10]These authors contributed equally
[11]Lead contact
*Correspondence: c.sacristan@hubrecht.eu (C.S.), kumiko.samejima@ed.ac.uk (K.S.), bill.earnshaw@ed.ac.uk (W.C.E.), g.kops@hubrecht.eu (G.J.P.L.K.)
https://doi.org/10.1016/j.cell.2024.04.014

SUMMARY

Centromeres are scaffolds for the assembly of kinetochores that ensure chromosome segregation during cell division. How vertebrate centromeres obtain a three-dimensional structure to accomplish their primary function is unclear. Using super-resolution imaging, capture-C, and polymer modeling, we show that vertebrate centromeres are partitioned by condensins into two subdomains during mitosis. The bipartite structure is found in human, mouse, and chicken cells and is therefore a fundamental feature of vertebrate centromeres. Super-resolution imaging and electron tomography reveal that bipartite centromeres assemble bipartite kinetochores, with each subdomain binding a distinct microtubule bundle. Cohesin links the centromere subdomains, limiting their separation in response to spindle forces and avoiding merotelic kinetochore-spindle attachments. Lagging chromosomes during cancer cell divisions frequently have merotelic attachments in which the centromere subdomains are separated and bioriented. Our work reveals a fundamental aspect of vertebrate centromere biology with implications for understanding the mechanisms that guarantee faithful chromosome segregation.

INTRODUCTION

During cell division, spindle microtubules attach to chromosomes at centromeres, specialized regions responsible for kinetochore assembly and epigenetically defined by the histone H3 variant CENP-A.[1,2] Vertebrate chromosomes have "regional" centromeres, which are usually enriched for high-copy number tandemly repeated satellite sequences associated into domains known as higher order repeats (HORs).[1–3] Satellite repeats, however, are not essential for centromere formation, as evolutionarily new centromeres occupy non-repetitive regions in several species, including chickens and equines,[4–7] and neocentromeres are observed in humans in rare cases.[1,2,8]

The CENP-A-enriched core centromere associates with the constitutive centromere-associated network (CCAN) to build the kinetochore[1] and is flanked by pericentromeres rich in methylated DNA and lacking CENP-A. CENP-A nucleosomes in the core centromere are interspersed with canonical histone H3-containing nucleosomes.[9] CENP-A nucleosomes of the core centromere pack into an as-yet unknown higher-order organization.[2,3,10] Current models assume that centromeric chromatin scaffolds a compact kinetochore structure that binds a single bundle of microtubules (the kinetochore fiber, or k-fiber) in mitosis.[3,9,11,12] This organization is thought to provide rigidity to the kinetochore, allowing biorientation and promoting faithful chromosome segregation.

The structural maintenance of chromosomes (SMCs) family of proteins are essential drivers of the three-dimensional (3D) chromatin organization[13,14] and important regulators of centromeres. Pericentromeric cohesin keeps sister chromatids tethered

Please cite this article in press as: Sacristan et al., Vertebrate centromeres in mitosis are functionally bipartite structures stabilized by cohesin, Cell (2024), https://doi.org/10.1016/j.cell.2024.04.014

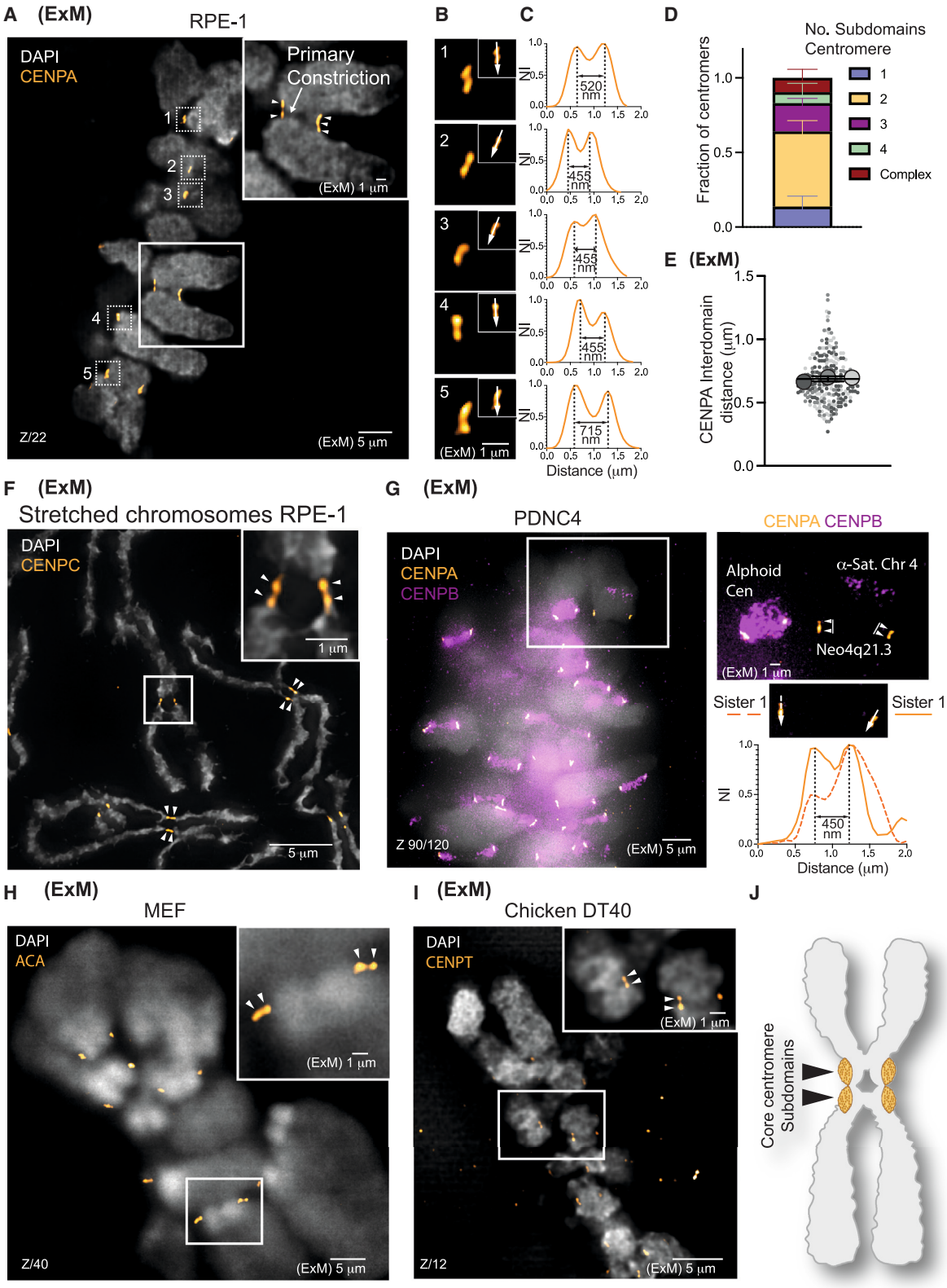

(legend on next page)

Please cite this article in press as: Sacristan et al., Vertebrate centromeres in mitosis are functionally bipartite structures stabilized by cohesin, Cell (2024), https://doi.org/10.1016/j.cell.2024.04.014

during cell division,[13–15] while condensin provides stiffness to the (peri)centromere.[16–18] Both are required to prevent the formation of merotelic attachments.[19–22] Although the role of SMC complexes in compaction of regional centromeres remains largely speculative, important insights have been obtained by studying the point centromere of *Saccharomyces cerevisiae*, with its single CENP-A nucleosome. In *S. cerevisiae*, cohesin and condensin occupy distinct subdomains of the pericentromere.[23,24] In one recent model, the pericentromere forms a bottlebrush consisting of arrays of loops cross-linked by cohesin, which is responsible both for keeping sister chromatids together and for cross-linking the arrays of loops extruded by condensin.[25,26] The cross-linked loops enable centromeres to resist spindle forces.

Here we investigated the higher-order organization of regional vertebrate centromeres and its functional consequences on kinetochore formation, spindle assembly, and chromosome segregation.

RESULTS

Regional centromeres in vertebrates are organized in two main subdomains in mitosis

To better understand the structural organization of the vertebrate core centromere, we performed super-resolution (expansion) microscopy (ExM)[27] of RPE-1 cells immunostained for CENP-A. Consistent with previous multi-unit centromere architecture models,[9,11,28] we observed that the core centromere is subdivided into discrete domains (Figures 1A–1C and S1A–S1E). Quantification revealed that most centromeres exhibited a bipartite organization (Figures 1D and S1A), with an estimated average inter-subdomain distance (center-to-center) of ~150–170 nm (~680 nm in 4- to 4.5-fold-expanded samples, Figure 1E). A similar CENP-A organization was seen by stimulated emission depletion (STED) microscopy of fixed HCT116 cells and by instant structured illumination microscopy (iSIM) of living U2OS cells expressing mCherry-CENP-A (Figures S1F–S1I), ruling out artifacts from gel expansion, fixation conditions, antibody staining, or cell type differences. Importantly, in centromeres having more than two subdomains, these subdomains tended to cluster into two main groups (Figure S1E). We conclude that most, if not all, centromeres of RPE-1 cells have a bipartite higher-order architecture.

Consistently, centromeres of stretched chromosomes (see STAR Methods) tended to split into two subdomains, each associated with a proximal chromosome arm (Figure 1F), similar to observations made during the first description of centromere protein antigens.[29] ExM imaging of normal chromosomes likewise showed, in cases where the shape of the chromosome was clearly visible, that the continuity of the CENP-A region was interrupted by the primary constriction (inset in Figure 1A).

ExM imaging of a patient-derived neocentromere that formed on non-repetitive sequences of chromosome 4 (PDNC4),[8] of mouse embryonic fibroblasts (with telocentric chromosomes),[30] and of chicken DT40 cells (which have repetitive and non-repetitive centromere sequences)[4] all showed bipartite centromere organization (Figures 1G–1I and S1J). Thus, centromeric chromatin has a conserved, bipartite higher-order organization with two major domains associated with the proximal chromosome arms regardless of underlying sequence and chromosomal position (Figure 1J).

Evidence of bipartite centromeric chromatin organization of the chicken Z-centromere from capture-C sequencing

Chicken DT40 cells have a single Z chromosome with a non-repetitive centromere (Zcen).[4] This enables unambiguous analysis of chromatin interactions by chromosome conformation capture techniques. We previously used chemical genetics and Hi-C sequencing of DT40 cells to reveal a substantial change of chromatin higher-order packing at centromeres during a highly synchronous transition from G_2 into mitosis[31] (Figures 2A and S2A). To better understand this change, we used capture-C, which can resolve structural details over genomic regions the size of chicken centromeres (tens of kilobases).[32] We visualized the data by plotting relative directionality of interactions over a range of distances from each genomic viewpoint.

Capture-C analysis of a region of 3–250 kb flanking the Zcen (Figure 2B) revealed that although core centromeric chromatin in G_2 cells tended to interact locally, the flanking pericentromeric chromatin preferentially interacted away from the core

Figure 1. Subdomain organization of the vertebrate regional centromere

(A–C) ExM (CENP-A, DAPI) of a metaphase RPE-1 cell. Arrowheads in inset: CENP-A subdomains.

(B) Blow-ups of the dotted boxes in (A).

(C) Line intensity profiles across centromere subdomains in (B). Distance between peaks is indicated.

(D) Fraction of centromeres per cell with the indicated number of CENP-A subdomains. Complex: centromeres with >4 subunits or heterogeneous shapes (mean ± SD of 4 independent experiments; $n = 21$ cells, 829 centromeres).

(E) Distance between CENP-A subdomains in bipartite centromeres in ExM images (mean ± SD of 3 independent experiments, $n = 240$ centromeres). Large dots, independent experiments; small dots, single centromeres.

(F) CENP-C immunostaining in stretched chromosomes. Arrowheads: CENP-C subdomains.

(G) (Left) ExM image of CENP-A and CENP-B in PDNC4 cells with neocentromere in chromosome 4 (Neo4q21.3).[8] (Right) Blow-up of the box in (G). Neo4q21.3 is recognized by the lack of CENP-B signal between sister centromeres; alphoid cen: a canonical centromere containing α-satellite repeats. Arrowheads: CENP-A subdomains.

(H) ExM (ACA, anti-centromere antibody) of mouse embryonic fibroblast (MEF). Arrowheads: ACA subdomains. See also Figure S1J.

(I) ExM (CENP-T) of a chicken DT40 cell. Arrowheads: CENP-T subdomains.

(J) Cartoon depicting core centromere organization. Two subdomains (orange balls) are each associated to one chromosome arm. In all figures, NI, normalized intensity; Z, plane of z stack or maximum intensity projection of indicated planes.

See also Figure S1.

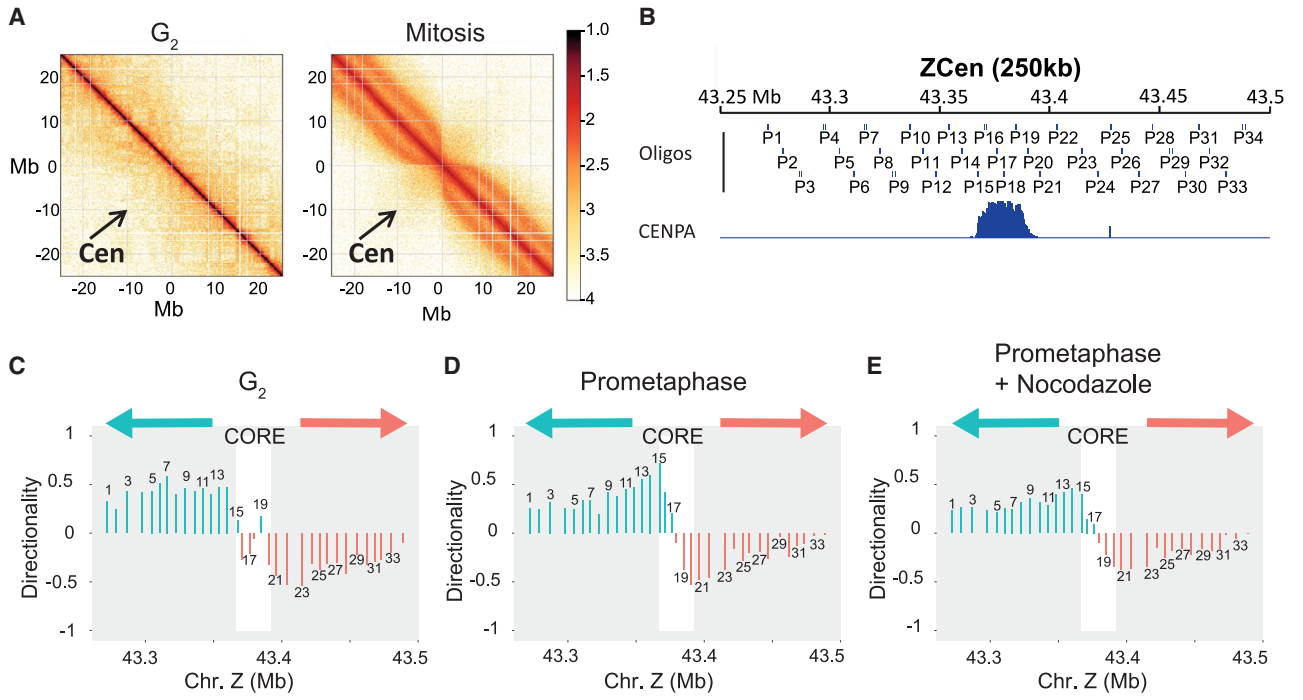

Figure 2. Bipartite mitotic centromeric chromatin organization of chicken Zcen

(A) Hi-C map of 25 Mbp region surrounding Zcen (arrow) in G_2 or in late prometaphase (T = 30 min after release from 1NM-PP1). 100 kb resolution. Data are from Gibcus et al.[31]

(B) Positions of capture oligo pairs (view points) (P1–P34) surrounding Zcen and the CENP-A ChIP-seq data to indicate the position of Z core centromere in wild-type (WT) CDK1^{as} parental cell line used for this study.

(C–E) Directionality of interactions at each view point in WT G_2 cells (C), WT late prometaphase cells (D), and WT late prometaphase cells treated with nocodazole (E). Core centromere (CENP-A region) is marked by white box. Asymmetry of interaction is depicted by green upward bar (more interactions toward p arm) and by orange downward bar (more interactions toward q arm). x axis shows genomic DNA position on Z chromosome. Value on the y axis is the natural log of the number of interactions toward the p arm divided by the number of interactions toward the q arm. Only interactions with positions within a distance of 3–250 kbp of the viewpoint are included. The graph represents sum of two independent experiments.

See also Figure S2.

centromere (Figure 2C). The core centromere thus forms a boundary, limiting interactions between p- and q-arm pericentromeres during interphase. Mitotic centromere chromatin, by contrast, adopted a striking left-right bipartite asymmetry centered within the CENP-A core (Figure 2D). This did not require kinetochore-microtubule interactions (Figure 2E) and was independent of underlying DNA sequence, as shown by analyzing a clone in which centromere position had "drifted"[33] by 10 kb (Figures S2B, S2D, and S2E). Moreover, an identical transition could be seen on the non-repetitive centromere of acrocentric chromosome 5 (5cen) (Figures S2C, S2G, and S2H). The directionality of left-right interactions was highest at the boundary between the CENP-A core and pericentromere and decreased for viewpoints moving away from the core (Figures 2D, 2E, S2E, and S2H). We therefore conclude that centromeric chromatin is reorganized as G_2 cells enter mitosis in a manner consistent with the bipartite structure observed by super-resolution imaging. This involves the loss of intra-core looping interactions and the establishment of a sharp boundary that limits interactions between chromatin domains on either side of the boundary and favors asymmetrical contacts outward toward the adjacent pericentromere regions.

Kinetochores are bipartite structures with subdomains that independently bind microtubule bundles

To explore how the bipartite organization of centromeric chromatin impacts kinetochore structure and function, we performed ExM on RPE-1 cells immunostained for α-tubulin and the CCAN component CENP-C. Although CENP-C staining generally appeared more complex than CENP-A (e.g., example 1 in Figures 3A and 3B), an underlying bipartite configuration was visible in 40% of kinetochores (Figures 3A–3C). A bipartite kinetochore was also seen when immunoimaging the microtubule-binding outer-kinetochore protein HEC1 (Figures 4B–4D).

Close inspection of the kinetochore-microtubule interface revealed that k-fibers rarely appeared as one compact bundle but instead were often comprised of distinct sub-bundles (Figures 3A, 3B, and S3A–S3D). Quantification of the number of bundles per k-fiber in ExM images showed that more than 50% of the kinetochores were attached to two main microtubule bundles (Figures 3C, 3D, and S3A–S3D). Quantitative analysis of 3D reconstructions of k-fibers obtained by electron tomography of HeLa cells[34] confirmed that most consisted of two discrete microtubule bundles (Figures 3E, 3F, and S3E–S3G). Double bundles within the same k-fiber were separated by an average

Please cite this article in press as: Sacristan et al., Vertebrate centromeres in mitosis are functionally bipartite structures stabilized by cohesin, Cell (2024), https://doi.org/10.1016/j.cell.2024.04.014

CellPress
OPEN ACCESS

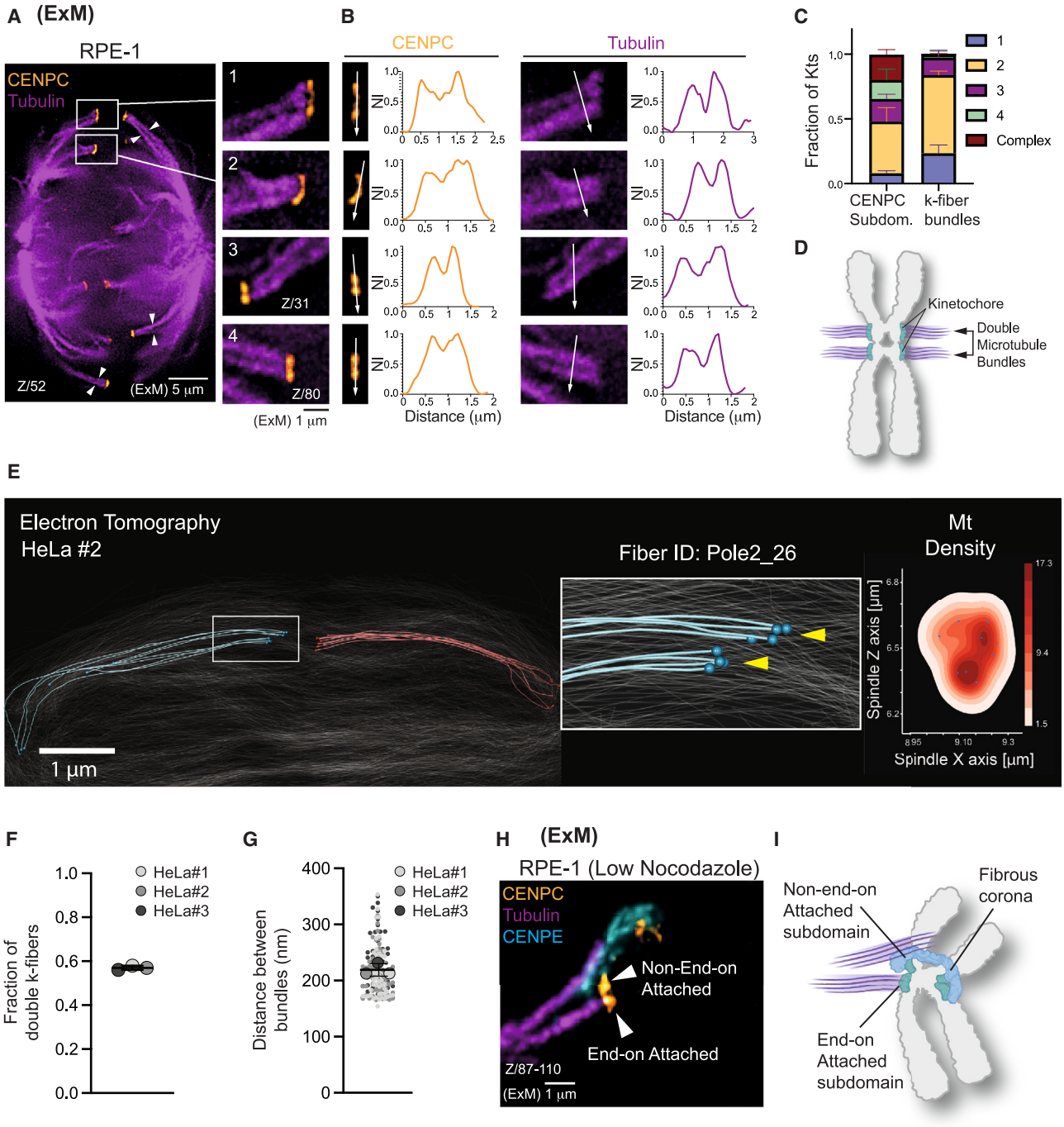

Figure 3. Kinetochore subdomains bind separate microtubule bundles

(A and B) ExM (α-tubulin, CENP-C) of metaphase RPE-1 cell cold-treated before fixation (A). (Right) Blow-ups of the boxes and other regions of the indicated planes. Arrowheads: double k-fibers. (B) Line intensity profiles across kinetochore subdomains (arrows in CENP-C) and k-fibers (arrows in α-tubulin).

(C) Fraction of centromeres per cell with the indicated number of CENP-C subdomains and k-fiber bundles (mean ± SD of 2 independent experiments; $n = 11$ cells, 466 centromeres). See also Figure S3.

(D) Cartoon depicting the binding of independent microtubule bundles (purple filaments) to kinetochore subdomains (green balls).

(E–G) 3D electron-tomography reconstruction showing k-fibers in HeLa cells (E). Blow-up, k-fiber with two microtubule bundles (yellow arrowheads), with the plus ends indicated with dark blue spheres. (Right) Kernel distance estimation plot of plus-end distribution along the xz axis. Fraction of k-fibers containing two distinct bundles (F). Average distance between the centers of masses of double bundles (G). (Mean ± SD, $n = 3$ cells, 289 k-fibers.) Analyses performed on data generated in Kiewisz et al.[34]

(legend continued on next page)

Please cite this article in press as: Sacristan et al., Vertebrate centromeres in mitosis are functionally bipartite structures stabilized by cohesin, Cell (2024), https://doi.org/10.1016/j.cell.2024.04.014

distance of 220 nm (Figure 3G), consistent with the estimated distance separating centromere subdomains. Of note, *Haemanthus* kinetochores have been reported to connect to "double fibers."[36] Thus, the bipartite organization of the centromere defines two microtubule-binding units. These units can act autonomously: delaying spindle assembly by low-dose nocodazole permitted us to observe kinetochores in which one subdomain was end-on attached while the other remained covered by the fibrous corona, an outer-kinetochore structure that is removed when end-on attachments are formed[35] (Figures 3H and 3I).

Biorientation of kinetochore subdomains is a common feature of merotelic kinetochore-spindle attachments

We next wondered if bipartite kinetochores are prone to form merotelic attachments, an erroneous configuration in which the kinetochore of one chromatid engages microtubules from both spindle poles, often causing the chromatid to lag behind in anaphase ("laggards").[19] In support of this, treating RPE-1 cells with the Aurora B inhibitor ZM-447439[37] resulted in stretched kinetochores with split CENP-C subdomains that were attached to microtubules from opposite spindle poles (Figure 4A). The two subdomains of bipartite kinetochores can therefore biorient and form merotelic attachments (Figure 4E). Further analysis of these merotelic attachments uncovered that they displayed a distinct configuration of inner- and outer-kinetochore proteins: condensin II (marked by CAP-H2) was flanked by two CENP-C subdomains that in turn were flanked by two HEC1 subdomains (examples 3 and 4 in Figures 4B–4D). By contrast, in correctly attached kinetochores (mono-oriented, i.e., single kinetochores with both subdomains connected to microtubules from the same pole), the two HEC1 subdomains remained closely associated and parallel to CENP-C and CAP-H2 (examples 1 and 2 in Figures 4B–4D). Therefore, merotely from bioriented subdomains can be readily identified by the specific arrangement of inner and outer layers of the kinetochore/centromere (Figure 4E). This enables quantification of merotely in any phase of mitosis.

We next used iSIM imaging to quantify merotelics. Although iSIM has lower resolution (~125 nm) than ExM and could not consistently resolve subdomains in normal mono-oriented kinetochores, it could distinguish separated HEC1 signals in single bioriented kinetochores and provided higher throughput than ExM. Using this approach, we detected a ~10-fold increase in the number of merotelic attachments when cells were treated with Aurora B inhibitor or were released from a monastrol-induced arrest[38] (Figures 4F–4H). Because this method of assessing merotely identifies only heavily stretched kinetochores, it therefore likely underestimates the actual number of merotelic events with bioriented subdomains. The distance between HEC1 subdomains in single bioriented kinetochores measured ~250–290 nm, compared with ~170–200 nm for mono-oriented kinetochores (Figure 4I). When assessing anaphase laggards in cells released from a monastrol arrest, a remarkable 30% had bioriented kinetochores split by an average distance of almost 400 nm (Figures 4J–4L and S4A). Taken together, our results suggest that biorientation of the two subdomains is a fundamental configuration of merotelically attached kinetochores, ultimately leading to anaphase laggards with hyper-stretched kinetochores.

Lagging chromosomes in cancer cells result from biorientation of kinetochore subdomains

Lagging chromosomes are the most common type of chromosome segregation error of cancer cells,[39] and we therefore wished to examine whether biorientation of kinetochore subdomains might be a natural cause of chromosomal instability (CIN) in cancer. Live-cell STED microscopy of U2OS cells (osteosarcoma) and immunostainings of OVSAHO (high-grade serous ovarian cancer), both with high rates of lagging chromosomes,[40,41] confirmed the presence of merotelic attachments with bioriented subdomains (Figures 5A, S4B, and S4C). ~50% of lagging chromatids of U2OS cells imaged live by iSIM showed split CENP-A signals (Figures 5B, 5C, and S4D–S4F; Video S1). Consistently, most metaphase U2OS cells (~60%) had at least one kinetochore with bioriented subdomains (Figures 5D, 5E, S4G, and S4H).

Patient-derived colorectal tumor organoid (PDO) retain functional and phenotype characteristics of the tumors they were derived from.[42] Analysis of PDO line P9T, which has high CIN rates and high frequency of lagging chromosomes,[43] showed that ~30% of lagging chromatids in anaphase displayed clear biorientation of the two centromere subdomains (Figures 5F, 5G, and S4A), and half of the metaphase cells showed at least one bioriented kinetochore (Figures 5E and 5H). Strikingly, the subdomains of bioriented kinetochores were substantially more separated in P9T cells (~320 nm) than in U2OS cells (~250 nm) (Figure 5I), suggesting destabilization of the bipartite centromere architecture in P9T.

Together, our findings demonstrate that merotely resulting from the biorientation of kinetochore subdomains is a frequent event in cancer cell divisions and a potential source of CIN.

A polymer model of bipartite centromere architecture

To find potential mechanisms that could lead to organization of centromeric chromatin into a structurally and functionally bipartite configuration, we designed a simple polymer model simulation (Figures 6A and S5A; STAR Methods). In this simulation, multivalent protein bridges, e.g., provided by SMC complexes,[44] bind either pericentromeric or centromeric chromatin and have a defined rate of switching from a binding to a non-binding state and vice versa. Switching could be driven by a nonequilibrium biochemical reaction of the proteins such as ATP hydrolysis.[45] The simulation (model 1) approximated the overall shape of the capture-C directionality plot (Figure S5A), provided that the binding affinity of bridging proteins to pericentromeres was larger than to the middle of the core centromere (the internal 11 kbp

(H) ExM of a bipartite kinetochore (CENP-C), with one subdomain end-on attached and the other laterally attached via the fibrous corona (marked by CENP-E[35]). The cell was treated with 330 nM nocodazole.
(I) Cartoon of image in (H).
See also Figure S3.

Please cite this article in press as: Sacristan et al., Vertebrate centromeres in mitosis are functionally bipartite structures stabilized by cohesin, Cell (2024), https://doi.org/10.1016/j.cell.2024.04.014

CellPress
OPEN ACCESS

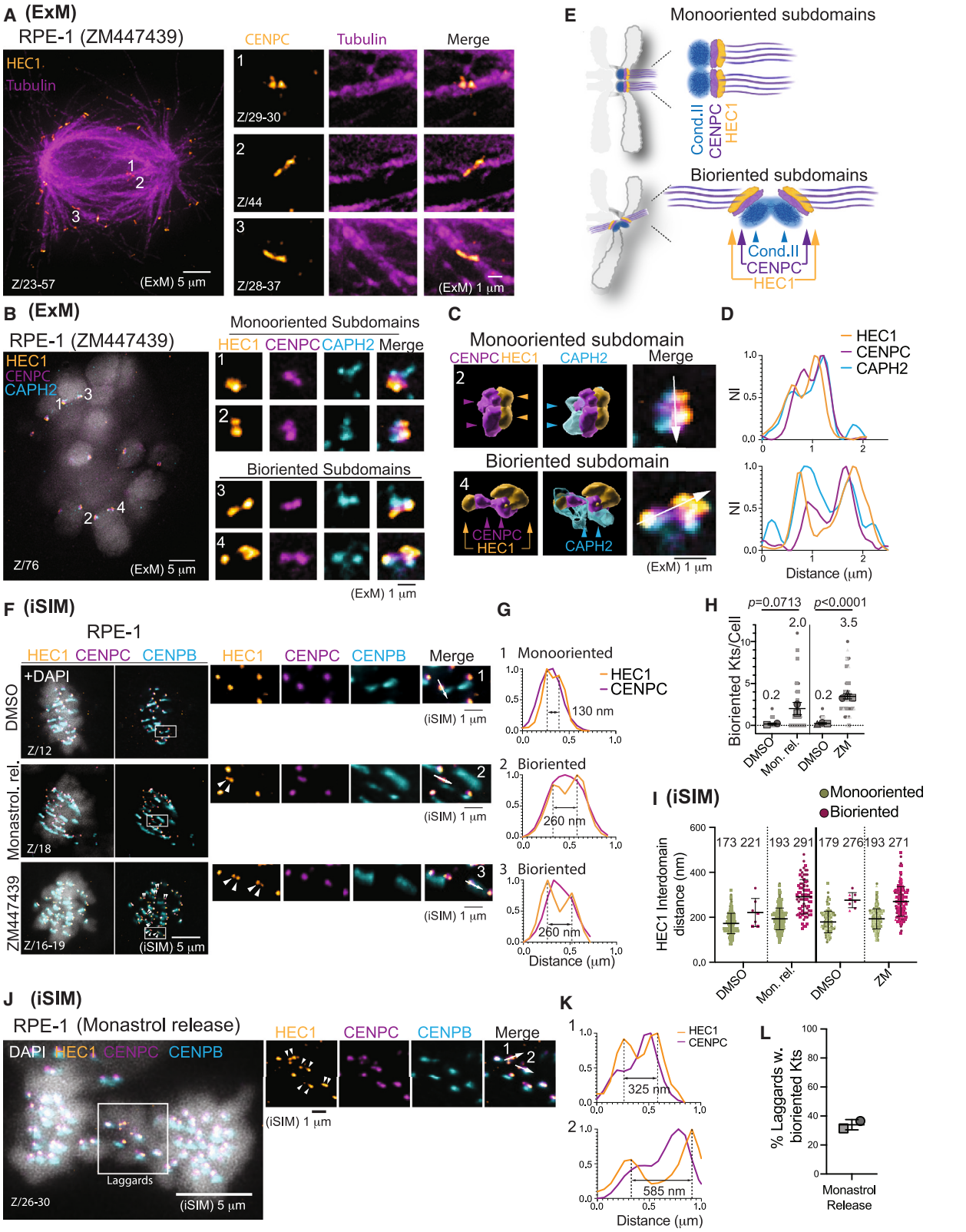

(legend on next page)

region) (compare with model 0 (Figure S5A), which has a lower binding affinity of SMC complexes for the pericentromere).

The chromatin in the model 1 simulation formed a spherical globule with the two pericentromere regions occupying two different hemispheres and the centromere on the surface (Figure S5A). Increasing the rate of switching of the bridges between binding or non-binding states (model 2) led to splitting of the globule in a significant portion of the simulated structures while retaining a significant asymmetry in the contact pattern as observed by capture-C (Figures S5A and S5B). Interestingly, introduction of loops within the model pericentromere (e.g., cohesin or condensin-mediated[31,46,47]), as described for yeast centromeres,[24–26,48] resulted in a more robust bipartite structure with enhanced directionality in the contacts and sharper transition between the two sides of the centromere, closely fitting our capture-C data (model 3; Figures 6A, 6B, and S5B).

Remarkably, the more complex capture-C patterns observed in G_2 could be reproduced by the addition of a second interphase-enriched bridging activity with preferential binding to the middle of the core centromere (e.g., cohesin), resulting in three main chromatin clusters (Figures 6A and 6C). These simulations thus indicate that binding of switchable cross-linking proteins combined with a bottlebrush folding of pericentromeric chromatin may be sufficient to explain the bipartite architecture of the core centromere.

Condensin II and cohesin accumulate proximally to the core centromere in mitosis

The polymer model and previous work in budding yeast that showed distinct pericentromeric distribution of SMC complexes[23,25] inspired us to assess their localization in vertebrate centromeres. We visualized cohesin and condensin by generating cells co-expressing SMC3-TurboID[49] (cohesin) and SMC2-mAID-mCherry[50] (condensin). Cohesin localization was determined by imaging biotinylated substrates in nocodazole-treated cells using ExM with partial (~2×) gel expansion. Partial expansion was required to retain sufficiently high signal intensity, and although it was insufficient to resolve centromere subdomains, it achieved enhanced spatial resolution of cohesin (Figures 6D, 6E, 6H, S6A, and S6B). A large pool of cohesin was observed flanking the kinetochore along the chromosome axis (marked by SMC2) (asterisks in Figures 6E, S6A, and S6B), which was reminiscent of the inner centromere protein INCENP[51] and is consistent with the expected role of cohesin in tethering sister chromatids near pericentromeric regions.[24,52] Notably, and consistent with recent findings,[52] our approach uncovered a second pool of cohesin proximal to the CENP-A region (yellow arrowheads in Figures 6E, S6A, and S6B).

In our images, SMC2 (common to condensin I/II) appeared much more enriched in the centromere compared with the rest of the chromosome (Figures 6D and 6E). Quantitative chromatin immunoprecipitation sequencing (ChIP-seq) analysis of chicken Zcen and 5cen confirmed this (Figures 6F, S6C, and S6D), but also revealed notable differences in their relative levels and distribution: CAP-H2 was ~20-fold enriched at the core centromere, compared with ~9-fold enrichment of condensin I (Figure S6C). Furthermore, in mitosis, condensin II reproducibly accumulated in two "cat's ears" peaks aligning with the edges of the core centromere (Figure 6F). Consistent with the ChIP-seq data, ExM of CAP-H2 confirmed that condensin II displays a bipartite configuration in mitotic chromosomes (Figures 4C, 4D, 6G, and 6H).

Condensin is required for organizing bipartite centromeres in mitosis

Condensin is required for normal compliance (elasticity) of centromeric heterochromatin in response to microtubule forces.[16–18,20,21,53] Indeed, CENP-A appeared stretched and heavily fragmented in metaphase cells depleted of the condensin subunit SMC2 in the presence (Figure 6I) and absence (Figure S6E) of microtubules. Capture-C analysis of DT40 cells acutely depleted of condensin showed that while G_2 cells maintained a wild-type chromatin folding and interaction profile (Figure S6F), the bipartite structural transformation of centromeric

Figure 4. Biorientation of kinetochore subdomains in merotelic attachments

(A) ExM image (α-tubulin, CENP-C) of an RPE-1 cell treated with ZM-447439. Blow-ups, merotelically attached kinetochores, where subdomains engage microtubules from opposite spindle poles.

(B–D) ExM image (HEC1, CENP-C, CAP-H2) of an RPE-1 cell treated with ZM-744439 (B). Blow-ups, mono-oriented kinetochores, where both subdomains face the same spindle pole, and bioriented kinetochores with subdomains oriented toward opposite poles. (C) 3D reconstructions and (D) line intensity profiles across kinetochores 2 and 4. In bioriented kinetochores, CENP-C localizes between HEC-1 subdomains.

(E) Cartoon depicting the relative distribution of HEC1, CENP-C, and CAP-H2 in mono-oriented and bioriented subdomains.

(F and G) iSIM images (HEC1, CENP-C, CENP-B) of RPE-1 cells released from monastrol or treated with ZM-447439 (F). Arrowheads: stretched bioriented subdomains. Line intensity profiles across kinetochore subdomains (G).

(H) Quantifications of the number of bioriented kinetochores per cell after monastrol release (mean ± SD of 2 independent experiments; DMSO: $n = 38$ cells, Mon. rel.: $n = 41$ cells; Student's t test, two-tailed, unpaired) or ZM-447439 treatment (mean ± SD of 3 independent experiments: DMSO: $n = 30$ cells, ZM: $n = 45$ cells; Student's t test, two-tailed, unpaired. p values are indicated). Large dots, independent experiments; small dots, single cells.

(I) Distance between HEC1 subdomains in mono-oriented and stretched kinetochores. Monastrol release (left) (mean ± SD, pooled kinetochores, 2 independent experiments; $DMSO^{Mono\text{-}oriented}$, $n = 323$, $DMSO^{Bioriented}$, $n = 7$; $Mon.\ rel.^{Mono\text{-}oriented}$, $n = 348$, $Mon.\ rel.^{Bioriented}$ $n = 75$). ZM-447439 treatment (right) (mean ± SD, pooled kinetochores, 3 independent experiments; $DMSO^{Mono\text{-}oriented}$, $n = 134$, $DMSO^{Bioriented}$, $n = 8$; $ZM^{Mono\text{-}oriented}$, $n = 189$, $ZM^{Bioriented}$, $n = 151$). Dots, single kinetochores.

(J) iSIM image of an anaphase RPE-1 cell after monastrol release and stained with the indicated antibodies. Blow-up, lagging chromosomes with bioriented subdomains (arrowheads).

(K) Line intensity profiles across kinetochore subdomains.

(L) Percentage of lagging chromosomes with bioriented kinetochores (mean ± SD of 2 independent experiments: $n = 180$ laggards from 42 cells). Dots, independent experiments. Quantifications of the distance between subdomains are shown in Figure S4A.

See also Figure S4.

Please cite this article in press as: Sacristan et al., Vertebrate centromeres in mitosis are functionally bipartite structures stabilized by cohesin, Cell (2024), https://doi.org/10.1016/j.cell.2024.04.014

CellPress
OPEN ACCESS

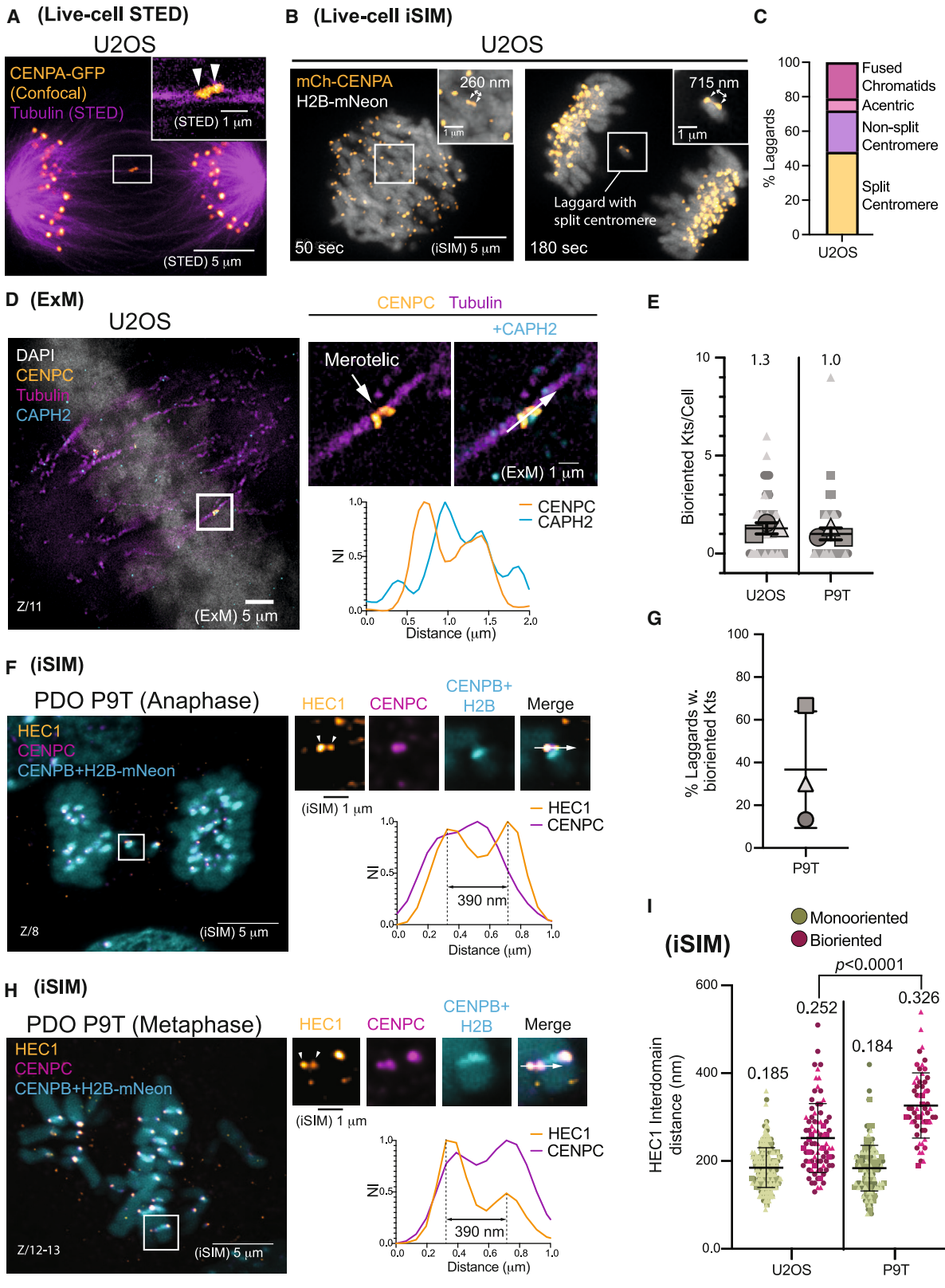

(legend on next page)

Please cite this article in press as: Sacristan et al., Vertebrate centromeres in mitosis are functionally bipartite structures stabilized by cohesin, Cell (2024), https://doi.org/10.1016/j.cell.2024.04.014

chromatin upon mitotic entry was abolished (Figure 6J). When microtubules were present, the interaction pattern looked chaotic, probably because microtubule-based movements effectively disrupt the kinetochore chromatin folding (Figure 6J). When condensin-depleted cells entered mitosis in the absence of microtubules, the mitotic Zcen had an organization indistinguishable from that of G_2 cells (Figure S6G). By contrast, lack of cohesin (SMC3 depletion) did not alter the folding of the Zcen in either G_2 or mitosis (Figures 6K and S2F–S2H).

Thus, condensin but not cohesin is essential for establishing the bipartite centromere organization in mitotic cells.

Cohesin stabilizes centromere subdomains and prevents merotelic attachments

Given the presence of a pool of cohesin proximal to the core centromere[52] (Figure 6E), we re-visited our polymer model simulation. Model 3 closely reproduced our capture-C data and was consistent with the observed distribution of condensin II, peaking at both edges of the core centromere. However, performing *in silico* ChIP for condensin II in model 3 predicted that much less condensin II would be present in between the two main peaks than observed in our experimental ChIP-seq data (Figure S5C vs. Figure 6F). When moderate levels of cohesin affinity for the central core centromere (2.5 times lower than in G_2) were incorporated into model 3 (Figures 7A–7C), condensin II was redistributed toward the middle of the core, generating a ChIP-seq pattern that recapitulated the observed ''cat's ears'' distribution and closely matching the capture-C data (Figure S5C). This modified model also predicted a higher dynamic correlation (correlated movement) between centromeric regions separated by more than 15 kb (Figures 7D, S5D, and S5E).

To build on the predictions from polymer modeling that cohesin contributes to physically and functionally coupling the two centromere subdomains, we examined the role of cohesin in maintaining the architectural integrity of the centromere.[24,26] Degron-mediated acute depletion of Sororin,[54] a protector of centromeric cohesin from WAPL-mediated release,[55,56] caused a pronounced reduction of both pools of cohesin (Figures S7A–S7C) and a cohesion fatigue phenotype (Video S2), with single chromatids misaligned at spindle poles (arrows in Figure 7E). Strikingly, many single chromatids managed to congress. These congressed chromatids had split kinetochores with merotelic spindle interactions, resulting in single chromatid biorientation (Figures 7E and S7D). Visualization of CAP-H2, which was located between CENP-C signals, verified that bioriented kinetochores represented single split centromeres rather than sister centromeres (Figures 7E, S7D, and S7E). Similar results were seen upon RNAi of RAD21, the kleisin subunit of cohesin[55] (Figure 7F).

The merotely phenotype after Sororin depletion was severe in cells stuck in mitosis for lengthy periods, exhibiting more than 50 split kinetochores per cell (Figures 7G–7I). Subdomains of these merotelically attached kinetochores were separated by distances often exceeding 500 nm (Figure 7L). The increased separation of subdomains in the absence of Sororin suggests a role of cohesin in physically tethering the two centromere subdomains to limit their separation under the strain of spindle forces. Supporting this, the degree of subdomain separation was significantly lower when merotelic attachments were induced by other means, such as inhibition of Aurora B kinase or depletion of Kif18A[57] (Figures 7J–7L and S7F–S7H). Conversely, depletion of WAPL enhanced cohesin levels on mitotic chromatin, including centromeres, and caused a modest but reproducibly significant reduction in the distance between subdomains (Figures 7M, 7N, S7I, and S7J).

Together, the combination of modeling and experimental data supports the hypothesis that cohesin stabilizes bipartite centromeres, resisting subdomain separation in response to spindle forces, and thereby promoting correct orientation of sister chromatids (Figure 7O).

DISCUSSION

At centromeres, a compact chromatin core enriched in CENP-A nucleosomes is flanked by heterochromatic pericentromeres. Here we find that the CENP-A core domain can reproducibly be resolved into two subdomains, each of which appears to be closely associated with its adjacent pericentromere. Not all

Figure 5. Lagging chromosomes in cancer cells result from the biorientation of kinetochore subdomains

(A) Live-cell imaging of a lagging chromosome in U2OS cell expressing CENP-A-GFP (confocal) and stained with SiR-tubulin (STED). Blow-up, two CENP-A domains (arrowheads) of a single centromere attached to microtubules from opposite spindle poles.

(B) iSIM movie of a U2OS cell showing a lagging chromosome with a centromere that splits as anaphase progresses. Arrowheads: split CENP-A signal. The distance between subdomains is shown. See also Video S1.

(C) Quantification of the frequencies of each type of lagging chromosome. See statistics and specific examples in Figures S4D–S4F.

(D) ExM image of a metaphase U2OS cell immunostained with the indicated antibodies. Blow-up, merotelic attachment with bioriented subdomains. Graph: line intensity profile across centromere subdomains.

(E) Quantifications of the number of bioriented kinetochores per cell in U2OS and P9T cells (mean ± SD, 3 independent experiments; U2OS $n = 56$ cells, P9T $n = 63$ cells). Large dots, independent experiments; small dots, single cells. See also Figures S4G and S4H.

(F) iSIM image of an anaphase P9T cell stained with the indicated antibodies. Blow-up, a lagging chromosome with bioriented subdomains (arrowheads). The graph depicts the line intensity profile across centromere subdomains.

(G) Percentage of lagging chromosomes in P9T cells with bioriented kinetochores (mean ± SD of 3 independent experiments; $n = 63$ laggers from 24 cells). Dots, independent experiments.

(H) iSIM image of a metaphase P9T cell stained with the indicated antibodies. Blow-up, sister kinetochores, the left one exhibits bioriented subdomains (arrowheads). The graph depicts the line intensity profile across centromere subdomains.

(I) Distance (iSIM microscopy) between HEC1 subdomains in mono-oriented and bioriented kinetochores in U2OS and P9T cells (mean ± SD from pooled kinetochores of 3 independent experiments; $U2OS^{Mono\text{-}oriented}$, $n = 306$; $U2OS^{Bioriented}$, $n = 83$; $P9T^{Mono\text{-}oriented}$, $n = 212$; $P9T^{Bioriented}$, $n = 59$. Student's t test, two-tailed, unpaired. p value is indicated). Dots, single kinetochores.

See also Figure S4.

Please cite this article in press as: Sacristan et al., Vertebrate centromeres in mitosis are functionally bipartite structures stabilized by cohesin, Cell (2024), https://doi.org/10.1016/j.cell.2024.04.014

CellPress
OPEN ACCESS

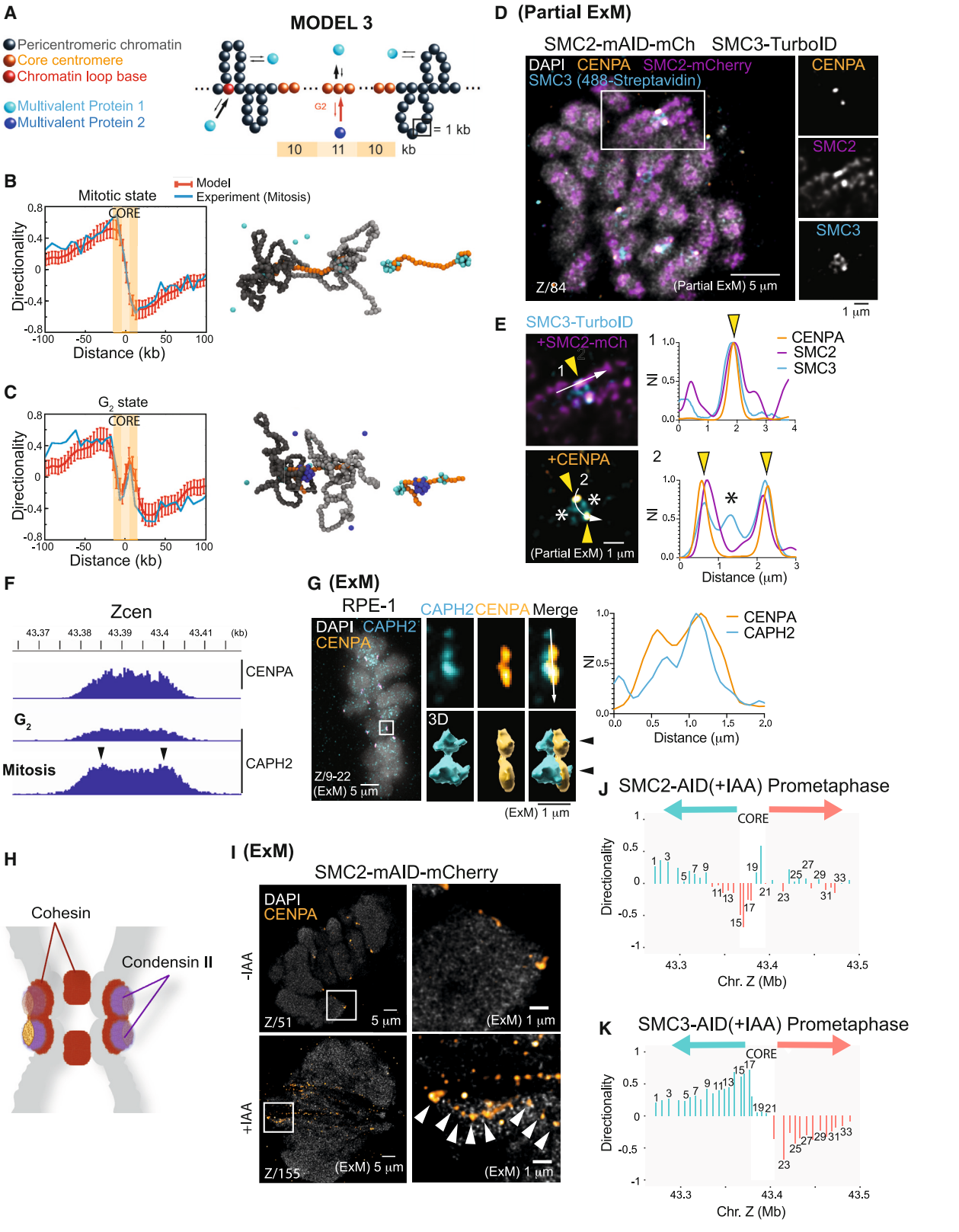

(legend on next page)

Please cite this article in press as: Sacristan et al., Vertebrate centromeres in mitosis are functionally bipartite structures stabilized by cohesin, Cell (2024), https://doi.org/10.1016/j.cell.2024.04.014

centromeres appear bipartite in our ExM analyses. This is likely due to insufficient resolution or heterogeneity of their orientation relative to the imaging axes. Indeed, in images of metaphase cells double-stained for CENP-A and tubulin, quantification of the number of centromeres that show either bipartite CENP-A foci and/or attachment to double k-fibers shows that at least 80% of the centromeres are bipartite (Figures S3C and S3D). This, together with our capture-C analysis (which is based on large populations of cells), suggests that bipartition is a consistent feature of vertebrate regional centromeres.

The pericentromere of *S. cerevisiae* is reported to adopt a bottlebrush-like configuration.[26,48] Interestingly, our modeling indicates that a bottlebrush architecture of the pericentromere can promote the partitioning of the core centromere into two major domains (Figures 6A and 6B). Although the presence of a single CENP-A nucleosome in budding yeast precludes a bipartite core centromere architecture, recent Hi-C analysis of yeast pericentromeres revealed, in striking similarity with our capture-C data, a tendency of the regions flanking the core centromere to interact with the pericentromere of the same arm.[24] Therefore, the bipartite organization of the vertebrate core centromere might reflect a conserved interaction with flanking pericentromeres, whose bottlebrush structure provides special mechanical properties to resist the pulling and pushing forces of microtubules.[26]

Our data indicate that the bipartite centromere architecture requires the function of condensin complexes during mitosis. The accumulation of CAP-H2 in two peaks at the edges of the core centromere observed by quantitative ChIP-seq suggests that condensin II is an important driver of bipartition. We hypothesize that epigenetic cues might orchestrate the localization of condensin II within the core centromere, thereby serving as primary delineators of the bipartite structure. The core and the pericentromere bear distinct marks of euchromatin and heterochromatin, respectively, with the core centromere exhibiting a dip in CpG methylation levels.[58,59] One of these marks, or their relative positioning, could dictate the accumulation of condensin II at the boundary between the core and the pericentromere. It will be important to examine how other mechanisms (e.g., binding of CCAN components,[28,60–62] CENP-B,[63] epigenetic marks, mitotic kinases) contribute to the organization of the bipartite chromatin structure.

The bipartite centromeric substructure impacts kinetochore function, as it creates two microtubule-binding interfaces that we have observed by both light microscopy and electron tomography. This changes our current understanding of spindle assembly and kinetochore regulation and may confer interesting advantages. For instance, two subdomains joined by a flexible linker could offer adaptability to the movement of highly dynamic microtubules, thereby alleviating strain imposed by geometrical positioning within the spindle and promoting sustained attachment. We also show that the subdomains are not necessarily simultaneously engaged to microtubules (Figure 3H), perhaps enhancing the efficiency of error correction and attachment maturation. Destabilization of merotelic attachments by Aurora B could selectively occur in one subdomain while enabling the other to maintain spindle connections. Future investigations into the behavior of bipartite microtubule-binding sites will likely require combinations of computational modeling and ways to experimentally fuse the two subdomains without altering other aspects of centromeres and kinetochores.

An important finding we report here and which is in agreement with recent work[52] is the existence of a cohesin pool proximal to the core centromere that we speculate may be responsible for keeping subdomains tethered (Figure 7O), for instance by cross-linking the loops formed by condensin, as proposed for budding yeast centromeres.[26] The fact that this pool is sensitive to Sororin depletion may, counter-intuitively, indicate that it is topologically loaded, mediating interactions in *trans*.[54] The location of the core centromere pool of cohesin, however, is more compatible with interactions occurring within the same

Figure 6. Condensin drives the partitioning of the centromere in mitosis

(A) Polymer model 3 incorporates two types of multivalent chromatin-binding proteins (MP1 and MP2). The core centromere consists of 31 kb, featuring a middle region (light orange) of 11 kb with distinct affinities for MP1 and MP2 compared with the flanking regions. MP1 exhibits a higher affinity for pericentromeric regions and the borders of the core centromere (dark orange) than for the core centromere (CM). This model also includes chromatin loops, which arise due to the higher affinity of MP1 at the base, an example of which is colored in red. These loops exclusively form in the pericentromere arms, creating a bottlebrush topology. MP2 binds the core centromere and is present only in G_2.

(B and C) Capture-C-like asymmetry plots (left panels) and typical 3D configurations obtained in equilibrium (right panels) in a mitotic- (B) and G_2-like (C) state of model 3. See Figure S5 and STAR Methods for more details.

(D and E) ExM (~2× expansion) of HCT-116 cell expressing SMC2-mAID-mCherry and SMC3-TurboID, and stained as indicated (D). Blow-up of boxed chromosome is shown on the right and in (E). Cells were synchronized with thymidine, released in nocodazole, and treated with biotin for 30 min before fixation. Biotinylated substrates were visualized with AF488-streptavidin. (E) Blow-up and line intensity profiles across a chromosome arm (1) and sister centromeres (2) of the boxed chromosome in (D). Yellow arrowheads point to the pool of cohesin proximal to the core centromere, and asterisks indicate the pool of cohesin at the inner centromere. See also Figures S6A and S6B.

(F) ChIP-seq of CENP-A and CAP-H2 in G_2 and mitosis. Arrowheads indicate the two peaks of condensin at the borders of the CENP-A domain. Graph represents the sum of two independent experiments. See also Figure S6C.

(G) ExM (CAP-H2, CENP-A) of an RPE-1 cell in metaphase. Blow-ups and 3D reconstructions on the right show the bipartite organization of CAP-H2 and CENP-A (arrowheads). Graph depicts the line intensity profile across centromere subdomains.

(H) Cartoon illustrating the bipartite organization of condensin II and the presence of two cohesin pools.

(I) ExM images of CENP-A in HCT-116$^{SMC2\text{-}mAID\text{-}mCherry}$ cells prepared in the absence or presence of auxin (IAA). Arrowheads: highly fragmented CENP-A domain following SMC2 depletion. See also Figure S6E.

(J and K) Directionality of interactions at each view point in SMC2-AID (J) and SMC3-AID (K) late prometaphase cells treated with auxin. Details of plots are as in Figures 2C–2E. In SMC3-AID cells, this is shifted toward the q arm by ~10 kb compared with WT and SMC2-AID cells due to centromere drift in this clone. Graphs represent sum of two independent experiments. See also Figures S2B, S6F, and S6G.

See also Figures S2, S5, and S6.

Please cite this article in press as: Sacristan et al., Vertebrate centromeres in mitosis are functionally bipartite structures stabilized by cohesin, Cell (2024), https://doi.org/10.1016/j.cell.2024.04.014

CellPress
OPEN ACCESS

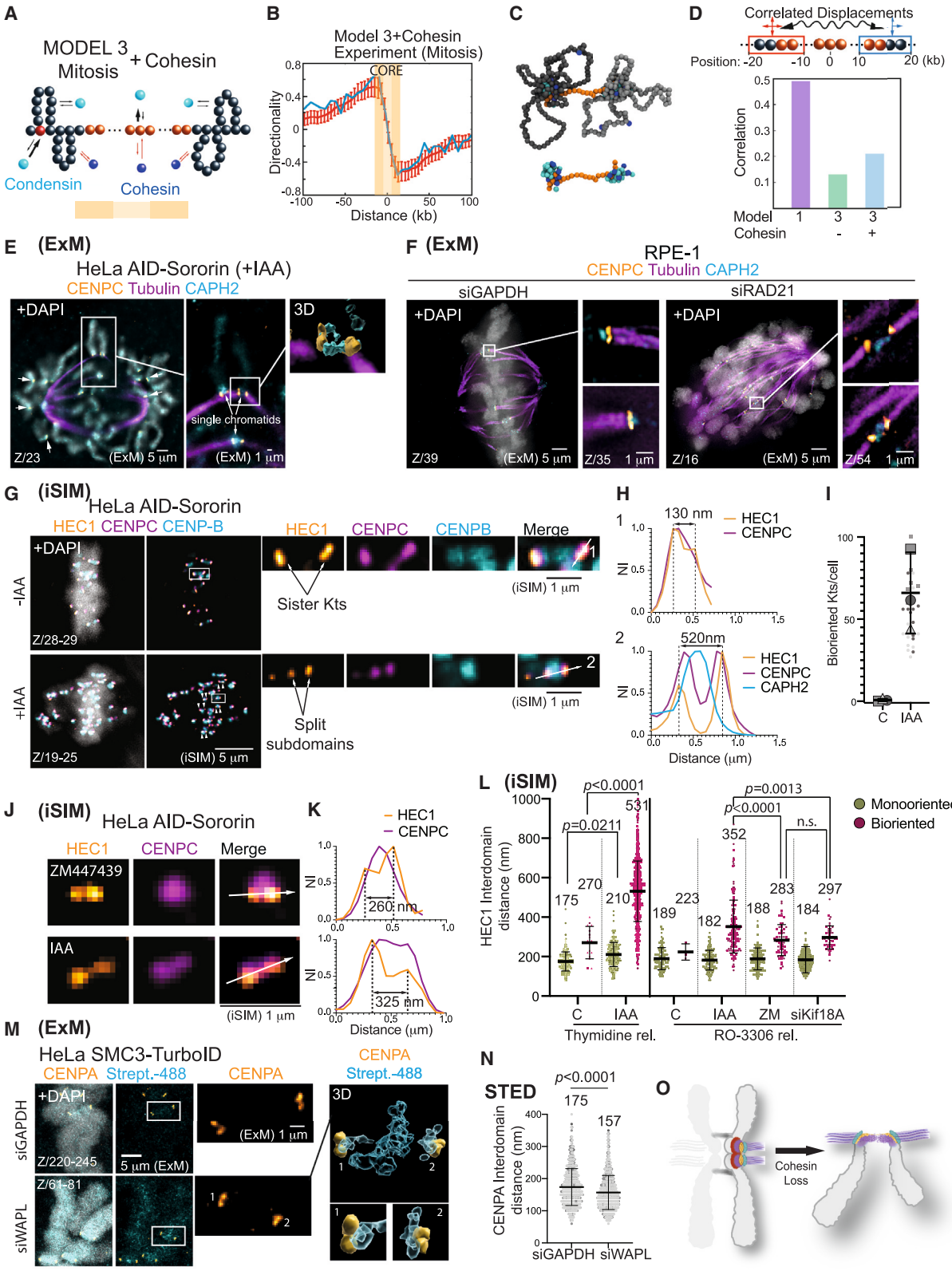

(legend on next page)

chromatid. Centromeric cohesin may thus have specialized properties, and further investigation is required to precisely determine the topological characteristics and centromeric distribution of this pool of cohesin. Notably, Sgo1 has also been observed in two pools at centromeres[64] and may thus also protect this secondary pool of cohesin from WAPL-mediated removal.

Cohesin depletion not only increases the number of merotelic attachments but also results in an extreme separation of bioriented subdomains, exceeding 500 nm after prolonged mitotic arrest (Figure 7H). The link between reduced cohesin levels, merotely, and kinetochore fragmentation in aging oocytes[22] further supports a pivotal role of cohesin in tethering centromere subdomains. Interestingly, merotelic attachments in the human colorectal cancer organoid line P9T have large subdomain distances resembling those of cohesin-depleted cells, suggesting that merotely in some cancers may be due to destabilization of centromere subdomain interactions. It will be important to examine how the mechanisms that ensure stability of the bipartite structure in healthy cells are compromised in chromosomally unstable cells in early development and cancer.

Limitations of the study

Our microscopy and capture-C approaches show that bipartition is a feature of centromeres of three vertebrate species, suggesting it is common among vertebrate centromeres. However, we cannot exclude the possibility that some vertebrates have a different centromere architecture. Furthermore, each subdomain may have a more complex substructure, as occasionally seen in our micrographs. Capture-C and ChIP-seq experiments rely on bulk input from many cells, and so they represent an average of many centromeres. Potential cell-to-cell variability in centromere configuration cannot be assessed by these methods. The localization of condensin and cohesin at the core centromere suggests these pools are involved in shaping the bipartite architecture, but until we specifically manipulate these pools, we cannot exclude more indirect contributions from other pools. Finally, our immunofluorescence method for detecting cohesin relies on proximity biotinylation, which can have off-target effects. However, our conclusions are in line with a recent study using direct immunolocalization.[52]

STAR★METHODS

Detailed methods are provided in the online version of this paper and include the following:

Figure 7. Cohesin stabilizes the bipartite centromere

(A–C) Polymer model 3 in mitosis incorporating moderate levels of cohesin (dark blue beads) (A). Capture-C-like asymmetry plots (B) and 3D configurations obtained in equilibrium (C). See Figure S5C and STAR Methods.

(D) Average correlation between the indicated regions of the centromere, with a lower correlation indicating greater independence between the left and right domains. See dynamic correlation matrix in Figure S5E.

(E) ExM image (CENP-C, α-tubulin, CAP-H2) of a HeLa$^{AID\text{-}Sororin}$ cell treated with auxin. Cells were cold-treated before fixation. Blow-up, three unpaired chromatids with split subdomains resulting from the formation of merotelic attachments, a 3D reconstruction of a singe kinetochore is shown in the right panel. Arrowheads: single chromatids. See also Figure S7D.

(F) ExM images (CENP-C, α-tubulin, CAP-H2) of cold-treated RPE1 cells treated with siGAPDH or siRAD21.

(G) iSIM images of HeLa$^{AID\text{-}Sororin}$ cells prepared in the absence or presence of auxin (IAA) and stained with the indicated antibodies. Arrowheads: split kinetochores.

(H) Line intensity profiles across kinetochore subdomains with the distance between peaks.

(I) Quantifications of the number of bioriented kinetochores per cell for the indicated treatments (mean ± SD of 3 independent experiments; control, $n = 33$ cells, IAA, $n = 36$ cells) large dots, independent experiments; small dots, single cells.

(J and K) iSIM images of bioriented subdomains in HeLa$^{AID\text{-}Sororin}$ cells treated with IAA or ZM-447439 (J) and line intensity profiles across centromere subdomains with the distance between peaks (K). Cells released from an RO-3306 arrest were fixed 1 h later. The corresponding cells are shown in Figure S7F.

(L) Distance (iSIM) between HEC1 subdomains in HeLa$^{AID\text{-}Sororin}$ cells treated as indicated (mean ± SD from pooled kinetochores. Thymidine release: 3 independent experiments; control$^{Mono\text{-}oriented}$, $n = 258$; control^{Bioriented}, $n = 16$; IAA$^{Mono\text{-}oriented}$, $n = 210$; IAA^{Bioriented}, $n = 1{,}180$; one-way ANOVA followed by Tukey's test. RO-3306 release: 2 independent experiments; control$^{Mono\text{-}oriented}$, $n = 118$; control^{Bioriented}, $n = 3$; IAA$^{Mono\text{-}oriented}$, $n = 126$; IAA^{Bioriented}, $n = 150$; ZM$^{Mono\text{-}oriented}$, $n = 105$; ZM^{Bioriented}, $n = 60$; siKif18A$^{Mono\text{-}oriented}$, $n = 178$; siKif18A^{Bioriented}, $n = 46$; one-way ANOVA followed by Tukey's test. p values are indicated). Dots, single kinetochores. See also Figure S7F.

(M) (Left) ExM images of HeLa$^{AID\text{-}Sororin\ SMC3\text{-}TurboID}$ cells transfected with siGAPDH or siWAPL and stained as indicated. (Right) 3D reconstruction of the pair of sister centromeres shown after siWAPL treatment.

(N) Distance (STED) between CENP-A subdomains in HeLa$^{AID\text{-}Sororin}$ cells treated with siGAPDH or siWAPL (mean ± SD from pooled kinetochores of 3 independent experiments. siGAPDH, $n = 816$; siWAPL, $n = 889$; Student's t test, two-tailed, unpaired. p value is indicated). Dots, single kinetochores. See Figure S7I.

(O) Cartoon depicting uncoupling of centromere subdomains and subsequent formation of merotelic attachments resulting from cohesin loss.

See also Figure S7.

SUPPLEMENTAL INFORMATION

Supplemental information can be found online at https://doi.org/10.1016/j.cell.2024.04.014.

ACKNOWLEDGMENTS

The work was funded by the European Research Council (ERC-SyG 855158 [G.J.P.L.K. and I.M.T.] and ERC-CoG 648050 [D.M.]), the Netherlands Organization for Scientific Research (NWO/OCENW.KLEIN.182 [G.J.P.L.K.]), the Wellcome Trust (Principal Research Fellowship 107022 [W.C.E.]), the UK Medical Research Council (MR/J00913X/1 and MC_UU_00007/13 [N.G.]), the Deutsche Forschungsgemeinschaft (MU 1423/8-2 and MU 1423/8-3, project no. 258577783 [T.M.-R.]), the Marie Skłodowska-Curie program (675737 [R.K. and T.M.-R.]), the Simons Foundation (SF349247 [R.K. and T.B.]), the Japan Science and Technology Agency (CREST, JPMJCR21E6 [T.F.]), and the Japan Society for the Promotion Science (JSPS) (20H05389, 21H05752, 22H00408, and 22H0469 [T.F.]). The Earnshaw lab is supported by the WCB bioinformatics core facility (core grant 203149 to the Wellcome Centre for Cell Biology). The Müller-Reichert lab acknowledges support from the CCBX program of the Center for Computational Biology of the Flatiron Institute (NY, USA). We thank Masatoshi Takagi, Daniel Gerlich, Ben Black, Masato Kanemaki, and Don Cleveland for reagents. We thank Abberior Instruments for imaging on the STEDYCON system and the Hubrecht Flow Cytometry Facility and Hubrecht Imaging Center for help. We thank Kops and Earnshaw lab members for discussions and comments on the manuscript. Figures 1J, 3D, 3I, 4E, 6H, and 7O were created with BioRender.com and modified with Adobe Illustrator.

AUTHOR CONTRIBUTIONS

C.S., K.S., W.C.E., N.G., and G.J.P.L.K. conceived the project. C.S., K.S., W.C.E., and G.J.P.L.K. wrote the manuscript. C.S. designed, performed, and analyzed microscopy experiments unless specified otherwise. K.S. and A.B. designed and performed capture-C experiments, which were analyzed by D.R. using software written and interpreted by C.A.B. L.A.R. and M.L.A.L. performed experiments in Figures 1G and 3H, respectively. D.M. designed and performed modeling experiments. T.H. and T.F. performed CENP-A ChIP-seq experiments, which were analyzed by S.W., K.S., and M.D. M.D. designed and performed condensin Halo ChIP-seq experiments, which were analyzed by S.W., M.D., and K.S. R.K. analyzed electron tomography data with the supervision of T.B. and T.M.-R. P.R. and K.V. conducted experiments in Figures 5A, S4B, and S4C, with the supervision of I.M.T. E.v.K. cultured and prepared P9T samples.

DECLARATION OF INTERESTS

The authors declare no competing interests.

Received: January 25, 2023
Revised: January 30, 2024
Accepted: April 14, 2024
Published: May 13, 2024

REFERENCES

1. McKinley, K.L., and Cheeseman, I.M. (2016). The molecular basis for centromere identity and function. Nat. Rev. Mol. Cell Biol. *17*, 16–29. https://doi.org/10.1038/nrm.2015.5.
2. Allshire, R.C., and Karpen, G.H. (2008). Epigenetic regulation of centromeric chromatin: old dogs, new tricks? Nat. Rev. Genet. *9*, 923–937. https://doi.org/10.1038/nrg2466.
3. Fukagawa, T., and Earnshaw, W.C. (2014). The centromere: chromatin foundation for the kinetochore machinery. Dev. Cell *30*, 496–508. https://doi.org/10.1016/j.devcel.2014.08.016.
4. Shang, W.-H., Hori, T., Toyoda, A., Kato, J., Popendorf, K., Sakakibara, Y., Fujiyama, A., and Fukagawa, T. (2010). Chickens possess centromeres with both extended tandem repeats and short non-tandem-repetitive sequences. Genome Res. *20*, 1219–1228. https://doi.org/10.1101/gr.106245.110.
5. Wade, C.M., Giulotto, E., Sigurdsson, S., Zoli, M., Gnerre, S., Imsland, F., Lear, T.L., Adelson, D.L., Bailey, E., Bellone, R.R., et al. (2009). Genome sequence, comparative analysis, and population genetics of the domestic horse. Science *326*, 865–867. https://doi.org/10.1126/science.1178158.
6. Nergadze, S.G., Piras, F.M., Gamba, R., Corbo, M., Cerutti, F., McCarter, J.G.W., Cappelletti, E., Gozzo, F., Harman, R.M., Antczak, D.F., et al. (2018). Birth, evolution, and transmission of satellite-free mammalian centromeric domains. Genome Res. *28*, 789–799. https://doi.org/10.1101/gr.231159.117.
7. Cappelletti, E., Piras, F.M., Sola, L., Santagostino, M., Abdelgadir, W.A., Raimondi, E., Lescai, F., Nergadze, S.G., and Giulotto, E. (2022). Robertsonian Fusion and Centromere Repositioning Contributed to the Formation of Satellite-free Centromeres during the Evolution of Zebras. Mol. Biol. Evol. *39*, msac162. https://doi.org/10.1093/molbev/msac162.
8. Amor, D.J., Bentley, K., Ryan, J., Perry, J., Wong, L., Slater, H., and Choo, K.H.A. (2004). Human centromere repositioning "in progress". Proc. Natl. Acad. Sci. USA *101*, 6542–6547. https://doi.org/10.1073/pnas.0308637101.
9. Blower, M.D., Sullivan, B.A., and Karpen, G.H. (2002). Conserved organization of centromeric chromatin in flies and humans. Dev. Cell *2*, 319–330. https://doi.org/10.1016/s1534-5807(02)00135-1.
10. Marshall, O.J., Marshall, A.T., and Choo, K.H.A. (2008). Three-dimensional localization of CENP-A suggests a complex higher order structure of centromeric chromatin. J. Cell Biol. *183*, 1193–1202. https://doi.org/10.1083/jcb.200804078.
11. Zinkowski, R.P., Meyne, J., and Brinkley, B.R. (1991). The centromere-kinetochore complex: a repeat subunit model. J. Cell Biol. *113*, 1091–1110. https://doi.org/10.1083/jcb.113.5.1091.
12. Ribeiro, S.A., Vagnarelli, P., Dong, Y., Hori, T., McEwen, B.F., Fukagawa, T., Flors, C., and Earnshaw, W.C. (2010). A super-resolution map of the vertebrate kinetochore. Proc. Natl. Acad. Sci. USA *107*, 10484–10489. https://doi.org/10.1073/pnas.1002325107.
13. Uhlmann, F. (2016). SMC complexes: from DNA to chromosomes. Nat. Rev. Mol. Cell Biol. *17*, 399–412. https://doi.org/10.1038/nrm.2016.30.
14. Yatskevich, S., Rhodes, J., and Nasmyth, K. (2019). Organization of Chromosomal DNA by SMC Complexes. Annu. Rev. Genet. *53*, 445–482. https://doi.org/10.1146/annurev-genet-112618-043633.
15. Michaelis, C., Ciosk, R., and Nasmyth, K. (1997). Cohesins: chromosomal proteins that prevent premature separation of sister chromatids. Cell *91*, 35–45. https://doi.org/10.1016/s0092-8674(01)80007-6.
16. Ribeiro, S.A., Gatlin, J.C., Dong, Y., Joglekar, A., Cameron, L., Hudson, D.F., Farr, C.J., McEwen, B.F., Salmon, E.D., Earnshaw, W.C., et al. (2009). Condensin regulates the stiffness of vertebrate centromeres. Mol. Biol. Cell *20*, 2371–2380. https://doi.org/10.1091/mbc.e08-11-1127.
17. Oliveira, R.A., Coelho, P.A., and Sunkel, C.E. (2005). The condensin I subunit Barren/CAP-H is essential for the structural integrity of centromeric heterochromatin during mitosis. Mol. Cell. Biol. *25*, 8971–8984. https://doi.org/10.1128/MCB.25.20.8971-8984.2005.
18. Gerlich, D., Hirota, T., Koch, B., Peters, J.-M., and Ellenberg, J. (2006). Condensin I stabilizes chromosomes mechanically through a dynamic interaction in live cells. Curr. Biol. *16*, 333–344. https://doi.org/10.1016/j.cub.2005.12.040.
19. Gregan, J., Polakova, S., Zhang, L., Tolić-Nørrelykke, I.M., and Cimini, D. (2011). Merotelic kinetochore attachment: Causes and effects. Trends Cell Biol. *21*, 374–381. https://doi.org/10.1016/j.tcb.2011.01.003.
20. Ono, T., Fang, Y., Spector, D.L., and Hirano, T. (2004). Spatial and temporal regulation of Condensins I and II in mitotic chromosome assembly in

human cells. Mol. Biol. Cell *15*, 3296–3308. https://doi.org/10.1091/mbc.e04-03-0242.

21. Samoshkin, A., Arnaoutov, A., Jansen, L.E.T., Ouspenski, I., Dye, L., Karpova, T., McNally, J., Dasso, M., Cleveland, D.W., and Strunnikov, A. (2009). Human condensin function is essential for centromeric chromatin assembly and proper sister kinetochore orientation. PLS One *4*, e6831. https://doi.org/10.1371/journal.pone.0006831.
22. Zielinska, A.P., Bellou, E., Sharma, N., Frombach, A.-S., Seres, K.B., Gruhn, J.R., Blayney, M., Eckel, H., Moltrecht, R., Elder, K., et al. (2019). Meiotic Kinetochores Fragment into Multiple Lobes upon Cohesin Loss in Aging Eggs. Curr. Biol. *29*, 3749–3765.e7. https://doi.org/10.1016/j.cub.2019.09.006.
23. Stephens, A.D., Quammen, C.W., Chang, B., Haase, J., Taylor, R.M., 2nd, and Bloom, K. (2013). The spatial segregation of pericentric cohesin and condensin in the mitotic spindle. Mol. Biol. Cell *24*, 3909–3919. https://doi.org/10.1091/mbc.E13-06-0325.
24. Paldi, F., Alver, B., Robertson, D., Schalbetter, S.A., Kerr, A., Kelly, D.A., Baxter, J., Neale, M.J., and Marston, A.L. (2020). Convergent genes shape budding yeast pericentromeres. Nature *582*, 119–123. https://doi.org/10.1038/s41586-020-2244-6.
25. Lawrimore, J., Doshi, A., Friedman, B., Yeh, E., and Bloom, K. (2018). Geometric partitioning of cohesin and condensin is a consequence of chromatin loops. Mol. Biol. Cell *29*, 2737–2750. https://doi.org/10.1091/mbc.E18-02-0131.
26. Lawrimore, J., and Bloom, K. (2022). Shaping centromeres to resist mitotic spindle forces. J. Cell Sci. *135*, jcs259532. https://doi.org/10.1242/jcs.259532.
27. Chen, F., Tillberg, P.W., and Boyden, E.S. (2015). Optical imaging. Expansion microscopy. Science *347*, 543–548. https://doi.org/10.1126/science.1260088.
28. Vargiu, G., Makarov, A.A., Allan, J., Fukagawa, T., Booth, D.G., and Earnshaw, W.C. (2017). Stepwise unfolding supports a subunit model for vertebrate kinetochores. Proc. Natl. Acad. Sci. USA *114*, 3133–3138. https://doi.org/10.1073/pnas.1614145114.
29. Earnshaw, W.C., and Rothfield, N. (1985). Identification of a family of human centromere proteins using autoimmune sera from patients with scleroderma. Chromosoma *91*, 313–321. https://doi.org/10.1007/BF00328227.
30. Kuznetsova, I., Podgornaya, O., and Ferguson-Smith, M.A. (2006). High-resolution organization of mouse centromeric and pericentromeric DNA. Cytogenet. Genome Res. *112*, 248–255. https://doi.org/10.1159/000089878.
31. Gibcus, J.H., Samejima, K., Goloborodko, A., Samejima, I., Naumova, N., Nuebler, J., Kanemaki, M.T., Xie, L., Paulson, J.R., Earnshaw, W.C., et al. (2018). A pathway for mitotic chromosome formation. Science *359*, eaao6135. https://doi.org/10.1126/science.aao6135.
32. Davies, J.O.J., Telenius, J.M., McGowan, S.J., Roberts, N.A., Taylor, S., Higgs, D.R., and Hughes, J.R. (2016). Multiplexed analysis of chromosome conformation at vastly improved sensitivity. Nat. Methods *13*, 74–80. https://doi.org/10.1038/nmeth.3664.
33. Hori, T., Kagawa, N., Toyoda, A., Fujiyama, A., Misu, S., Monma, N., Makino, F., Ikeo, K., and Fukagawa, T. (2017). Constitutive centromere-associated network controls centromere drift in vertebrate cells. J. Cell Biol. *216*, 101–113. https://doi.org/10.1083/JCB.201605001.
34. Kiewisz, R., Fabig, G., Conway, W., Baum, D., Needleman, D., and Müller-Reichert, T. (2022). Three-dimensional structure of kinetochore-fibers in human mitotic spindles. eLife *11*, e75459. https://doi.org/10.7554/eLife.75459.
35. Kops, G.J.P.L., and Gassmann, R. (2020). Crowning the Kinetochore: The Fibrous Corona in Chromosome Segregation. Trends Cell Biol. *30*, 653–667. https://doi.org/10.1016/j.tcb.2020.04.006.
36. Mole-Bajer, J., Bajer, A.S., Zinkowski, R.P., Balczon, R.D., and Brinkley, B.R. (1990). Autoantibodies from a patient with scleroderma CREST recognized kinetochores of the higher plant Haemanthus. Proc. Natl. Acad. Sci. USA *87*, 3599–3603. https://doi.org/10.1073/pnas.87.9.3599.
37. Cimini, D., Wan, X., Hirel, C.B., and Salmon, E.D. (2006). Aurora kinase promotes turnover of kinetochore microtubules to reduce chromosome segregation errors. Curr. Biol. *16*, 1711–1718. https://doi.org/10.1016/J.CUB.2006.07.022.
38. Lampson, M.A., Renduchitala, K., Khodjakov, A., and Kapoor, T.M. (2004). Correcting improper chromosome-spindle attachments during cell division. Nat. Cell Biol. *6*, 232–237. https://doi.org/10.1038/NCB1102.
39. Compton, D.A. (2011). Mechanisms of aneuploidy. Curr. Opin. Cell Biol. *23*, 109–113. https://doi.org/10.1016/J.CEB.2010.08.007.
40. Tamura, N., Shaikh, N., Muliaditan, D., Soliman, T.N., McGuinness, J.R., Maniati, E., Moralli, D., Durin, M.A., Green, C.M., Balkwill, F.R., et al. (2020). Specific Mechanisms of Chromosomal Instability Indicate Therapeutic Sensitivities in High-Grade Serous Ovarian Carcinoma. Cancer Res. *80*, 4946–4959. https://doi.org/10.1158/0008-5472.CAN-19-0852.
41. Bakhoum, S.F., Genovese, G., and Compton, D.A. (2009). Deviant kinetochore microtubule dynamics underlie chromosomal instability. Curr. Biol. *19*, 1937–1942. https://doi.org/10.1016/J.CUB.2009.09.055.
42. Van De Wetering, M., Francies, H.E., Francis, J.M., Bounova, G., Iorio, F., Pronk, A., Van Houdt, W., Van Gorp, J., Taylor-Weiner, A., Kester, L., et al. (2015). Prospective derivation of a living organoid biobank of colorectal cancer patients. Cell *161*, 933–945. https://doi.org/10.1016/J.CELL.2015.03.053.
43. Bolhaqueiro, A.C.F., Ponsioen, B., Bakker, B., Klaasen, S.J., Kucukkose, E., van Jaarsveld, R.H., Vivié, J., Verlaan-Klink, I., Hami, N., Spierings, D.C.J., et al. (2019). Ongoing chromosomal instability and karyotype evolution in human colorectal cancer organoids. Nat. Genet. *51*, 824–834. https://doi.org/10.1038/s41588-019-0399-6.
44. Ryu, J.-K., Bouchoux, C., Liu, H.W., Kim, E., Minamino, M., de Groot, R., Katan, A.J., Bonato, A., Marenduzzo, D., Michieletto, D., et al. (2021). Bridging-induced phase separation induced by cohesin SMC protein complexes. Sci. Adv. *7*, eabe5905. https://doi.org/10.1126/sciadv.abe5905.
45. Brackley, C.A., Liebchen, B., Michieletto, D., Mouvet, F., Cook, P.R., and Marenduzzo, D. (2017). Ephemeral Protein Binding to DNA Shapes Stable Nuclear Bodies and Chromatin Domains. Biophys. J. *112*, 1085–1093. https://doi.org/10.1016/j.bpj.2017.01.025.
46. Fudenberg, G., Imakaev, M., Lu, C., Goloborodko, A., Abdennur, N., and Mirny, L.A. (2016). Formation of Chromosomal Domains by Loop Extrusion. Cell Rep. *15*, 2038–2049. https://doi.org/10.1016/j.celrep.2016.04.085.
47. Oldenkamp, R., and Rowland, B.D. (2022). A walk through the SMC cycle: From catching DNAs to shaping the genome. Mol. Cell *82*, 1616–1630. https://doi.org/10.1016/j.molcel.2022.04.006.
48. Lawrimore, J., Aicher, J.K., Hahn, P., Fulp, A., Kompa, B., Vicci, L., Falvo, M., Taylor, R.M., and Bloom, K. (2016). ChromoShake: a chromosome dynamics simulator reveals that chromatin loops stiffen centromeric chromatin. Mol. Biol. Cell *27*, 153–166. https://doi.org/10.1091/mbc.E15-08-0575.
49. Branon, T.C., Bosch, J.A., Sanchez, A.D., Udeshi, N.D., Svinkina, T., Carr, S.A., Feldman, J.L., Perrimon, N., and Ting, A.Y. (2018). Efficient proximity labeling in living cells and organisms with TurboID. Nat. Biotechnol. *36*, 880–887. https://doi.org/10.1038/nbt.4201.
50. Takagi, M., Ono, T., Natsume, T., Sakamoto, C., Nakao, M., Saitoh, N., Kanemaki, M.T., Hirano, T., and Imamoto, N. (2018). Ki-67 and condensins support the integrity of mitotic chromosomes through distinct mechanisms. J. Cell Sci. *131*, jcs212092. https://doi.org/10.1242/jcs.212092.
51. Ainsztein, A.M., Kandels-Lewis, S.E., Mackay, A.M., and Earnshaw, W.C. (1998). INCENP centromere and spindle targeting: identification of essential conserved motifs and involvement of heterochromatin protein HP1. J. Cell Biol. *143*, 1763–1774. https://doi.org/10.1083/jcb.143.7.1763.

52. Sen Gupta, A., Seidel, C., Tsuchiya, D., McKinney, S., Yu, Z., Smith, S.E., Unruh, J.R., and Gerton, J.L. (2023). Defining a core configuration for human centromeres during mitosis. Nat. Commun. *14*, 7947. https://doi.org/10.1038/S41467-023-42980-2.

53. Samejima, K., Booth, D.G., Ogawa, H., Paulson, J.R., Xie, L., Watson, C.A., Platani, M., Kanemaki, M.T., and Earnshaw, W.C. (2018). Functional analysis after rapid degradation of condensins and 3D-EM reveals chromatin volume is uncoupled from chromosome architecture in mitosis. J. Cell Sci. *131*, jcs210187. https://doi.org/10.1242/jcs.210187.

54. Mitter, M., Gasser, C., Takacs, Z., Langer, C.C.H., Tang, W., Jessberger, G., Beales, C.T., Neuner, E., Ameres, S.L., Peters, J.-M., et al. (2020). Conformation of sister chromatids in the replicated human genome. Nature *586*, 139–144. https://doi.org/10.1038/s41586-020-2744-4.

55. Haarhuis, J.H.I., Elbatsh, A.M.O., and Rowland, B.D. (2014). Cohesin and its regulation: on the logic of X-shaped chromosomes. Dev. Cell *31*, 7–18. https://doi.org/10.1016/j.devcel.2014.09.010.

56. Nishiyama, T., Ladurner, R., Schmitz, J., Kreidl, E., Schleiffer, A., Bhaskara, V., Bando, M., Shirahige, K., Hyman, A.A., Mechtler, K., et al. (2010). Sororin mediates sister chromatid cohesion by antagonizing Wapl. Cell *143*, 737–749. https://doi.org/10.1016/j.cell.2010.10.031.

57. Stumpff, J., von Dassow, G., Wagenbach, M., Asbury, C., and Wordeman, L. (2008). The kinesin-8 motor Kif18A suppresses kinetochore movements to control mitotic chromosome alignment. Dev. Cell *14*, 252–262. https://doi.org/10.1016/J.DEVCEL.2007.11.014.

58. Altemose, N., Logsdon, G.A., Bzikadze, A.V., Sidhwani, P., Langley, S.A., Caldas, G.V., Hoyt, S.J., Uralsky, L., Ryabov, F.D., Shew, C.J., et al. (2022). Complete genomic and epigenetic maps of human centromeres. Science *376*, eabl4178. https://doi.org/10.1126/science.abl4178.

59. Gershman, A., Sauria, M.E.G., Guitart, X., Vollger, M.R., Hook, P.W., Hoyt, S.J., Jain, M., Shumate, A., Razaghi, R., Koren, S., et al. (2022). Epigenetic patterns in a complete human genome. Science *376*, eabj5089. https://doi.org/10.1126/science.abj5089.

60. Zhou, K., Gebala, M., Woods, D., Sundararajan, K., Edwards, G., Krzizike, D., Wereszczynski, J., Straight, A.F., and Luger, K. (2022). CENP-N promotes the compaction of centromeric chromatin. Nat. Struct. Mol. Biol. *29*, 403–413. https://doi.org/10.1038/s41594-022-00758-y.

61. Melters, D.P., Pitman, M., Rakshit, T., Dimitriadis, E.K., Bui, M., Papoian, G.A., and Dalal, Y. (2019). Intrinsic elasticity of nucleosomes is encoded by histone variants and calibrated by their binding partners. Proc. Natl. Acad. Sci. USA *116*, 24066–24074. https://doi.org/10.1073/pnas.1911880116.

62. Hara, M., Ariyoshi, M., Sano, T., Nozawa, R.S., Shinkai, S., Onami, S., Jansen, I., Hirota, T., and Fukagawa, T. (2023). Centromere/kinetochore is assembled through CENP-C oligomerization. Mol. Cell *83*, 2188–2205.e13. https://doi.org/10.1016/J.MOLCEL.2023.05.023.

63. Chardon, F., Japaridze, A., Witt, H., Velikovsky, L., Chakraborty, C., Wilhelm, T., Dumont, M., Yang, W., Kikuti, C., Gangnard, S., et al. (2022). CENP-B-mediated DNA loops regulate activity and stability of human centromeres. Mol. Cell *82*, 1751–1767.e8. https://doi.org/10.1016/j.molcel.2022.02.032.

64. Liu, H., Jia, L., and Yu, H. (2013). Phospho-H2A and cohesin specify distinct tension-regulated Sgo1 pools at kinetochores and inner centromeres. Curr. Biol. *23*, 1927–1933. https://doi.org/10.1016/J.CUB.2013.07.078.

65. Brown, K.D., Wood, K.W., and Cleveland, D.W. (1996). The kinesin-like protein CENP-E is kinetochore-associated throughout poleward chromosome segregation during anaphase-A. J. Cell Sci. *109*, 961–969. https://doi.org/10.1242/JCS.109.5.961.

66. Hori, T., Amano, M., Suzuki, A., Backer, C.B., Welburn, J.P., Dong, Y., McEwen, B.F., Shang, W.H., Suzuki, E., Okawa, K., et al. (2008). CCAN makes multiple contacts with centromeric DNA to provide distinct pathways to the outer kinetochore. Cell *135*, 1039–1052. https://doi.org/10.1016/J.CELL.2008.10.019.

67. Régnier, V., Novelli, J., Fukagawa, T., Vagnarelli, P., and Brown, W. (2003). Characterization of chicken CENP-A and comparative sequence analysis of vertebrate centromere-specific histone H3-like proteins. Gene *316*, 39–46. https://doi.org/10.1016/s0378-1119(03)00768-6.

68. van der Horst, A., Vromans, M.J.M., Bouwman, K., van der Waal, M.S., Hadders, M.A., and Lens, S.M.A. (2015). Inter-domain Cooperation in INCENP Promotes Aurora B Relocation from Centromeres to Microtubules. Cell Rep. *12*, 380–387. https://doi.org/10.1016/J.CELREP.2015.06.038.

69. Barisic, M., Silva e Sousa, R., Tripathy, S.K., Magiera, M.M., Zaytsev, A.V., Pereira, A.L., Janke, C., Grishchuk, E.L., and Maiato, H. (2015). Mitosis. Microtubule detyrosination guides chromosomes during mitosis. Science *348*, 799–803. https://doi.org/10.1126/SCIENCE.AAA5175.

70. Hasson, D., Panchenko, T., Salimian, K.J., Salman, M.U., Sekulic, N., Alonso, A., Warburton, P.E., and Black, B.E. (2013). The octamer is the major form of CENP-A nucleosomes at human centromeres. Nat. Struct. Mol. Biol. *20*, 687–695. https://doi.org/10.1038/nsmb.2562.

71. Hoevenaar, W.H.M., Janssen, A., Quirindongo, A.I., Ma, H., Klaasen, S.J., Teixeira, A., van Gerwen, B., Lansu, N., Morsink, F.H.M., Offerhaus, G.J.A., et al. (2020). Degree and site of chromosomal instability define its oncogenic potential. Nat. Commun. *11*, 1501. https://doi.org/10.1038/s41467-020-15279-9.

72. Sacristan, C., Ahmad, M.U.D., Keller, J., Fermie, J., Groenewold, V., Tromer, E., Fish, A., Melero, R., Carazo, J.M., Klumperman, J., et al. (2018). Dynamic kinetochore size regulation promotes microtubule capture and chromosome biorientation in mitosis. Nat. Cell Biol. *20*, 800–810. https://doi.org/10.1038/s41556-018-0130-3.

73. Janssen, L.M.E., Averink, T.V., Blomen, V.A., Brummelkamp, T.R., Medema, R.H., and Raaijmakers, J.A. (2018). Loss of Kif18A Results in Spindle Assembly Checkpoint Activation at Microtubule-Attached Kinetochores. Curr. Biol. *28*, 2685–2696.e4. https://doi.org/10.1016/J.CUB.2018.06.026.

74. Perez-Pinera, P., Kocak, D.D., Vockley, C.M., Adler, A.F., Kabadi, A.M., Polstein, L.R., Thakore, P.I., Glass, K.A., Ousterout, D.G., Leong, K.W., et al. (2013). RNA-guided gene activation by CRISPR-Cas9-based transcription factors. Nat. Methods *10*, 973–976. https://doi.org/10.1038/nmeth.2600.

75. Schmid-Burgk, J.L., Höning, K., Ebert, T.S., and Hornung, V. (2016). CRISPaint allows modular base-specific gene tagging using a ligase-4-dependent mechanism. Nat. Commun. *7*, 12338. https://doi.org/10.1038/ncomms12338.

76. Chien, J.C.Y., Tabet, E., Pinkham, K., da Hora, C.C., Chang, J.C.Y., Lin, S., Badr, C.E., and Lai, C.P.K. (2020). A multiplexed bioluminescent reporter for sensitive and non-invasive tracking of DNA double strand break repair dynamics in vitro and in vivo. Nucleic Acids Res. *48*, e100. https://doi.org/10.1093/NAR/GKAA669.

77. Drost, J., van Jaarsveld, R.H., Ponsioen, B., Zimberlin, C., van Boxtel, R., Buijs, A., Sachs, N., Overmeer, R.M., Offerhaus, G.J., Begthel, H., et al. (2015). Sequential cancer mutations in cultured human intestinal stem cells. Nature *521*, 43–47. https://doi.org/10.1038/nature14415.

78. Pemble, H., Kumar, P., van Haren, J., and Wittmann, T. (2017). GSK3-mediated CLASP2 phosphorylation modulates kinetochore dynamics. J. Cell Sci. *130*, 1404–1412. https://doi.org/10.1242/jcs.194662.

79. Bolger, A.M., Lohse, M., and Usadel, B. (2014). Trimmomatic: a flexible trimmer for Illumina sequence data. Bioinformatics *30*, 2114–2120. https://doi.org/10.1093/BIOINFORMATICS/BTU170.

80. Plimpton, S. (1995). Fast parallel algorithms for short-range molecular dynamics. J. Comput. Phys. *117*, 1–19. https://doi.org/10.1006/jcph.1995.1039.

81. Buckle, A., Gilbert, N., Marenduzzo, D., and Brackley, C.A. (2019). capC-MAP: software for analysis of Capture-C data. Bioinformatics *35*, 4773–4775. https://doi.org/10.1093/bioinformatics/btz480.

82. Samejima, K., Ogawa, H., Cooke, C.A., Hudson, D.F., Macisaac, F., Ribeiro, S.A., Vagnarelli, P., Cardinale, S., Kerr, A., Lai, F., et al. (2008). A promoter-hijack strategy for conditional shutdown of multiply spliced essential cell cycle genes. Proc. Natl. Acad. Sci. USA *105*, 2457–2462. https://doi.org/10.1073/pnas.0712083105.

83. Ran, F.A., Hsu, P.D., Wright, J., Agarwala, V., Scott, D.A., and Zhang, F. (2013). Genome engineering using the CRISPR-Cas9 system. Nat. Protoc. *8*, 2281–2308. https://doi.org/10.1038/nprot.2013.143.

84. Natsume, T., Kiyomitsu, T., Saga, Y., and Kanemaki, M.T. (2016). Rapid Protein Depletion in Human Cells by Auxin-Inducible Degron Tagging with Short Homology Donors. Cell Rep. *15*, 210–218. https://doi.org/10.1016/j.celrep.2016.03.001.

85. Vukušić, K., Ponjavić, I., Buđa, R., Risteski, P., and Tolić, I.M. (2021). Microtubule-sliding modules based on kinesins EG5 and PRC1-dependent KIF4A drive human spindle elongation. Dev. Cell *56*, 1253–1267.e10. https://doi.org/10.1016/J.DEVCEL.2021.04.005.

86. Brackey, C.A., Marenduzzo, D., and Gilbert, N. (2020). Mechanistic modeling of chromatin folding to understand function. Nat. Methods *17*, 767–775. https://doi.org/10.1038/s41592-020-0852-6.

87. Stoddard, S.D. (1978). Identifying clusters in computer experiments on systems of particles. J. Comp. Phys. *27*, 291–293. https://doi.org/10.1016/0021-9991(78)90011-6.

Please cite this article in press as: Sacristan et al., Vertebrate centromeres in mitosis are functionally bipartite structures stabilized by cohesin, Cell (2024), https://doi.org/10.1016/j.cell.2024.04.014

CellPress
OPEN ACCESS

STAR★METHODS

KEY RESOURCES TABLE

REAGENT or RESOURCE	SOURCE	IDENTIFIER
Antibodies		
Mouse anti-CENPA (3-19)	Enzo	Cat# ADI-Kam-CC006-E; RRID: AB_2038993
Guinea pig polyclonal anti-CENP-C	MBL	Cat# PD030; RRID: AB_10693556
Rabbit polyclonal anti-mCherry	Abcam	Cat# ab167453; RRID: AB_2571870
Mouse monoclonal anti α-tubulin (B-5-1-2)	Sigma-Aldrich	Cat# T5168; RRID: AB_477579
Rabbit polyclonal anti-N-CAP-H2	Abcam	Cat# ab221722; RRID:AB_3096900
Rabbit polyclonal anti-CENP-E	Prof. Don Cleveland; Brown et al.[65]	N/A
Anti-Human ANA-Centromere CREST	Bio connect/Fitzgerald	Cat# 90C-CS1058; RRID: AB_1282595
Rabbit polyclonal anti-CENP-T (Chicken)	Prof. Tatsuo Fukagawa;Hori et al.[66]	N/A
Rabbit polyclonal anti-CENP-A (Chicken)	Prof. William Brown; Regnier et al.[67]	N/A
Rabbit polyclonal anti-CENP-B	Abcam	Cat# ab25734; RRID: AB_726801
Mouse monoclonal anti-HEC1 (9G3.23)	Thermo Fisher Scientific	Cat# MA1-23308; RRID: AB_2149871
Rat monoclonal anti α-tubulin (B-5-1-2)	Thermo Fisher Scientific	Cat# MA1-80017; RRID: AB_2210201
Anti-Centromere Protein Antibody	Antibodies Incorporated	Cat# 15-234; RRID: AB_2939058
Rabbit polyclonal anti-Sgo2L	Novus	Cat# NB100-60454; RRID: AB_905750
Goat anti-guinea pig Alexa Fluor 488	Invitrogen Molecular Probes	Cat#A11073; RRID: AB_142018
Goat anti-rabbit Alexa Fluor 488	Invitrogen Molecular Probes	Cat# A11034; RRID: AB_2576217
Goat Anti-Human IgG Antibody, Alexa Fluor 568	Invitrogen Molecular Probes	Cat# A21090; RRID: AB_1500627
Goat Anti-mouse IgG (H+L), F(ab')2 Alexa Fluor 594	Cell Signaling Technology	Cat# 8890; RRID: AB_2714182
Goat Anti-rabbit IgG (H+L), F(ab')2 Alexa Fluor 594	Cell Signaling Technology	Cat# 8889; RRID: AB_2716249
Goat Anti-Mouse-IgG - Atto 647N	Sigma-Aldrich	Cat# 50185; RRID: AB_1137661
Goat Anti-Rabbit-IgG - Atto 647N	Sigma-Aldrich	Cat# 40839; RRID: AB_1137669
Goat Anti-mouse IgG Star Orange	Abberior	Cat# STORANGE-1001-500UG; RRID: AB_2847853
Goat Anti-mouse IgG Star Red	Abberior	Cat# STRED-1001-500UG; RRID: AB_3068620
Donkey Anti-Rat IgG H&L Alexa Fluor® 594	Abcam	Cat# ab150156; RRID: AB_2890252
Goat polyclonal Antibody to Human IgG H&L DyLight488	Abcam	Cat# ab96907; RRID: AB_10680094
Goat anti-guinea pig Alexa Fluor 647	Invitrogen Molecular Probes	Cat# A21450; RRID: AB_141882
Bacterial and virus strains		
E. coli Stbl3	Thermo Fisher Scientific	C737303
Biological samples		
Colon PDO – P9T H2B-mNeon	Hubrecht Organoid Technology (HUB) Foundation	Bolhaqueiro et al.[43]
Chemicals, peptides, and recombinant proteins		
Streptavidin, Alexa Fluor™ 488 conjugate	Thermo Fisher Scientific	Cat#S11223
RO-3306	Tocris Bioscience	Cat#4181
ZM-447439	Tocris Bioscience	Cat#2458
MG-132	Sigma-Aldrich	Cat#C2211
Thymidine	Sigma-Aldrich	Cat#T1895
Monastrol	Tocris Bioscience	Cat#1305
3-indoleacetic acid	Sigma-Aldrich	Cat#I5148
Biotin	Sigma-Aldrich	Cat#B4501
Doxycycline	Sigma-Aldrich	Cat#D9891

(*Continued on next page*)

Please cite this article in press as: Sacristan et al., Vertebrate centromeres in mitosis are functionally bipartite structures stabilized by cohesin, Cell (2024), https://doi.org/10.1016/j.cell.2024.04.014

Continued

REAGENT or RESOURCE	SOURCE	IDENTIFIER
Nocodazole	Sigma-Aldrich	Cat#M1404
1NM-PP1	Custom made	N/A
Chicken serum	Thermo Fisher Scientific	16110082
DMSO	Sigma-Aldrich	Cat#D8418
Hygromycin	Roche	Cat#10843555001
R-spondin 3 (Conditioned media)	ImmunoPrecise	N/A
Noggin (Conditioned media)	ImmunoPrecise	N/A
B27- supplement	Fisher Scientific	Cat#17504001
Nicotinamide	Sigma Aldrich	Cat#72340
N-acetylcysteine	Sigma Aldrich	Cat#A7250
A83-01	Tocris	Cat#2939
Human- EGF	Bio-Techne	Cat#236
SB203580	Sigma Aldrich	Cat#S7076
Y-27632 dihydrochloride	AbMole BioScience/Forlab	Cat#M1817
SiR-tubulin dye	Spirochrome AG	Cat# CY-SC002
Thermo Scientific™ Pierce™ 16% Formaldehyde (w/v), Methanol-free	Thermo Fisher Scientific	Cat#11586711
Glycine	Sigma-aldrich	Cat#G8790
Triton X-100	Sigma-aldrich	Cat#X100
20% SDS	Invitrogen	Cat#AM9820
UltraPure™ Tris	Invitrogen	Cat#15504020
DTT	Thermo Fisher Scientific	Cat#R0861
NaCl	Fisher Scientific	10428420
Hepes	Sigma-aldrich	Cat#H4034
Na-deoxycholate	Sigma-aldrich	Cat#D6750
Lithium chloride	Sigma-aldrich	Cat#310468
NP-40	Thermo Fisher Scientific	Cat#85124
SPRIselect Bead	Beckmen Coulter	Cat#B23318
Sodium bicarbonate	Sigma-aldrich	Cat#S5761
Sodium acetate	Sigma-aldrich	Cat#S2889
Proteinase K, recombinant, PCR Grade	Roche	Cat#RPROTKSOL-RO
Protease inhibitor cocktail	Sigma-aldrich	Cat#P8340
RNaseA	Thermo Fisher Scientific	Cat#EN0531
Nuclease free water	Beckmen Coulter	Cat#B23318
DPBS (1X)	Gibco	Cat#14190-094
Halo-Trap Agarose	Chromotek	Cat#ota-20
Ethanol absolute	Fisher Scientific	12478740
QIAquick PCR Purification Kit	Qiagen	Cat#28104
Agilent High Sensitivity DNA Kit	Agilent	Cat#5067-4626
ChromoTek Binding Control Agarose Beads	ChromoTek	Cat#bab
Tween 20	Merck	Cat#Bp337-100
Agarose	Sigma-aldrich	Cat#A9539
Geneticin	Thermo Fisher Scientific	Cat#10131035
DpnII	NEB	Cat#R0543M
T4 DNA ligase	NEB	Cat#M0202M
AM puro XP magnetic Beads	Beckman Coulter	Cat#A63881
EDTA free protease inhibitor	Roche	Cat#11836170001
T4 DNA ligase buffer	NEB	Cat#B0202S
RNase A/T1 cocktail	Thermo Fisher Scientific	Cat#EN0551

(*Continued on next page*)

Please cite this article in press as: Sacristan et al., Vertebrate centromeres in mitosis are functionally bipartite structures stabilized by cohesin, Cell (2024), https://doi.org/10.1016/j.cell.2024.04.014

Continued

REAGENT or RESOURCE	SOURCE	IDENTIFIER
Glycogen	Roche	Cat#10901393001
Igepal CA-630	Sigma-aldrich	Cat#13021-100ml
HCl (~37%)	Fisher Chemical	Cat#H/1200/PB17
Phenol/Chloroform/Isoamylalcohol mix	Sigma-aldrich	Cat#77617_500ml
Chloroform	Sigma-aldrich	Cat#650498
BSA	NEB	Cat#B9000S
Qubit dsDNA BR	Thermo Fisher Scientific	Cat#Q32853
Human cot1DNA	Thermo Fisher Scientific	Cat#15279-011
Q5 UltraII mater mix	NEB	Cat#M0544L
Dynabeads Myone StreptavidinT1	Thermo Fisher Scientific	Cat#65601
Critical commercial assays		
NEBNext® Multiplex Oligos for Illumina® (Index Primers Set 1)	NEB	Cat#E7335L
NEBNext® Multiplex Oligos for Illumina® (Index Primers Set 2)	NEB	Cat#E7500S
NEBNext® Ultra™ II DNA Library Prep Kit for Illumina®	NEB	Cat#E7645L
Neon™ Electroporation System	Thermo Fisher Scientific	Cat#NEON1
NimbleGen SeqCap EZ Hybridization and Wash Kits	Roche	Cat#5634261001
NimbleGen SeqCap EZ HE-Oligo Kit A	Roche	Cat#6777287001
NimbleGen SeqCap EZ HE-Oligo Kit B	Roche	Cat#6777317001
NimbleGen SeqCap EZ Accessory Kit v2	Roche	Cat#6776345001
Deposited data		
Chip-seq and Capture-C	GEO (GSE254182)	https://www.ncbi.nlm.nih.gov/geo/query/acc.cgi?acc=GSE254182
Experimental models: Cell lines		
RPE-1 FLPin hTERT	Laboratory of Jonathon Pines	N/A
U2OS	Laboratory of Susanne Lens	van der Horst et al.[68]
U2OS$^{CENP\text{-}A\text{-}GFP}$	Laboratory of Helder Maiato	Barisic et al.[69]
U2OS$^{CENP\text{-}A\text{-}GFP\ H2B\text{-}mNeon}$	This study	N/A
HCT-116$^{SMC2\text{-}mAID\text{-}mCherry}$	Laboratory of Masatoshi Takagi	Takagi et al.[50]
HCT-116$^{SMC2\text{-}mAID\text{-}mCherry\ /SMC3\text{-}TurboID}$	This study	N/A
PDNC4	Laboratory of Ben Black	Hasson et al.[70]
HeLa$^{EGFP\text{-}AID\text{-}Sororin}$	Laboratory of Daniel Gerlich	Mitter et al.[54]
HeLa$^{EGFP\text{-}AID\text{-}Sororin/SMC3\text{-}TurboID}$	This study	N/A
Mouse embryonic fibroblasts (*CiMKi*$^{wt/wt}$)	Laboratory of Geert Kops	Hoevenaar et al.[71]
HeLa FLPin$^{mCherry\text{-}Tubulin}$	Laboratory of Geert Kops	Sacristan et al.[72]
OVSAHO	JCRB Cell Bank	JCRB1046
DT40 WTCDK1^{as}	Laboratory of Bill Earnshaw	Gibcus et al.[31]
DT40 WTCDK1^{as}_TIR1 SMC2-AID	This study	N/A
DT40 WTCDK1^{as}_TIR1 SMC3-AID	This study	N/A
DT40 WTCDK1^{as}_TIR1 CAPH-HALO	This study	N/A
DT40 WTCDK1^{as}_TIR1 HALO-CAPH2	This study	N/A
Halo-Cid Schneider	This study	N/A
Oligonucleotides		
siGAPDH	Dharmacon	D-001830-01-05
siKif18A CCAACAACAGUGCCAUAAAUU	Dharmacon Custom	Janssen et al.[73]

(*Continued on next page*)

Please cite this article in press as: Sacristan et al., Vertebrate centromeres in mitosis are functionally bipartite structures stabilized by cohesin, Cell (2024), https://doi.org/10.1016/j.cell.2024.04.014

Continued

REAGENT or RESOURCE	SOURCE	IDENTIFIER
siRAD21 SMARTpool: ON-TARGET plus -J-006832-06: GCUCAGCCUUUGUGGAAUA- J-006832-07: GGGAGUAGUUCGAAUCUAU- J-006832-08: GACCAAGGUUCCAUAUUAU- J-006832-09: GCAUUGGAGCCUAUUGAUA	Dharmacon	L-006832-00-0010
siWAPL: GAGAGAUGUUUACGAGUUU	Dharmacon	J-026287-10
Primers for cloning	This paper	Table S1
Recombinant DNA		
pSPgRNA	Perez-Pinera et al.[74]	Addgene plasmid # 47108
pCS446_pSPgSMC3	This study	N/A
3xHA-TurboID-NLS_pCDNA3	Branon et al.[49]	Addgene plasmid #107171
pCRISPaint-mNeon	Schmid-Burgk et al.[75]	Addgene plasmid #174092
pCS452_pCRISPaint-TurboID-pPGK-Hygro	This study	N/A
pCAS9-mCherry-Frame+2	Schmid-Burgk et al.[75]	Addgene plasmid #66941
pX330	Chien et al.[76]	Addgene plasmid #158973
pLV-H2B-Neon-ires-Puro	Drost et al.[77]	
pLenti6-CENP-A-mCherry	Pemble et al.[78]	Addgene plasmid #89767
Software and algorithms		
ImageJ	NIH	https://imagej.nih.gov/ij/
Prism 9	GraphPad	https://www.graphpad.com/scientific-software/prism/
Imaris Software (v9.7.2)	Bitplane	https://imaris.oxinst.com/
Trimmomatic v0.36	Bolger et al.[79]	http://www.usadellab.org/cms/index.php?page=trimmomatic
BWA mem v0.7.16	Heng Li	https://github.com/lh3/bwa?tab=readme-ov-file
deepTools bamCoverage v3.5	deepTools	https://deeptools.readthedocs.io/en/develop/
LAMMPS	Plimpton[80]	https://github.com/lammps/lammps
Huygens Professional (v20.10)	Scientific Volume Imaging	https://svi.nl/Huygens-Professional
capC-MAP software	Buckle[81]	https://github.com/cbrackley/capC-MAP

RESOURCE AVAILABILITY

Lead contact

Further information and requests for resources and reagents should be directed to and will be fulfilled by the lead contact, Geert Kops (g.kops@hubrecht.eu).

Materials availability

All materials generated during the current study are available from the corresponding authors on reasonable request.

Data and code availability

- ChIP-seq and Capture-C data are publicly available in Gene Expression Omnibus database (GEO: GSE254182).
- This paper does not report original code. Datasets generated from LAMMPS simulations are available from the lead contact upon request.
- Any additional information required to reanalyze the data reported in this work paper is available from the lead contact upon request

EXPERIMENTAL MODEL AND STUDY PARTICIPANT DETAILS

RPE-1 cells (Flp-In) (a gift from the laboratory of J. Pines) were cultured in DMEM/F-12+GlutaMAX (Gibco, Cat# 31331-028) supplemented with 10% Tet-approved Fetal Bovine Serum (FBS) (Sigma-Aldrich, Cat# F7524) and 100 μg/ml penicillin/streptomycin

(Gibco, Cat# 15140-122) at 37 °C and 5% CO_2. U2OS (a gift from the Dr. Susanne Lens),[68] U2OS$^{CENP\text{-}A\text{-}GFP}$ (a gift from Dr. Helder Maiato),[69] PDNC4 (a gift from Dr. Ben Black),[70] HCT-116$^{SMC2\text{-}mAID\text{-}mCherry}$ (a gift from Dr. Masatoshi Takagi),[50] HeLa$^{EGFP\text{-}AID\text{-}Sororin}$ (a gift from Dr. Daniel Gerlich)[54] cells, mouse embryonic fibroblasts (*CiMKi*$^{wt/wt}$)[71] and HeLa FlpIn$^{mCherry\text{-}tubulin}$ [72]were cultured in DMEM (Gibco, Cat# 41966-029) supplemented with 10% Tet-approved FBS (Sigma-Aldrich, Cat# F7524), 100 μg/ml penicillin/streptomycin , and GlutaMAX supplement (Gibco, Cat# 35050-038). The OVSAHO cells (human ovarian carcinoma, female) (JCRB Cell Bank No. JCRB1046) were cultured in RPMI-1640 Medium with L-glutamine and sodium bicarbonate (Sigma-Aldrich, Cat# R8758) supplemented with 10% FBS (Sigma Aldrich, Cat# F2442), and a 100 μg/ml penicillin)/streptomycin (Gibco, Cat# 10378016). Chicken DT40 (B lymphoma) cells were cultured in RPMI1640 medium supplemented with 10 % fetal bovine serum and 1% chicken serum at 39°C in 5% CO_2 in air. Cells were confirmed to be mycoplasma negative.

METHOD DETAILS

Generation of stable cell lines

HCT-116$^{SMC2\text{-}mAID\text{-}mCherry/SMC3\text{-}TID}$ and HeLa$^{EGFP\text{-}AID\text{-}Sororin/SMC3\text{-}TID}$ cell lines are derived from HCT-116$^{SMC2\text{-}mAID\text{-}mCherry}$ and HeLa$^{EGFP\text{-}AID\text{-}Sororin}$, respectively. Tagging of the endogenous locus of SMC3 was done according to the CRISPaint protocol [75] using 2.5 μg frame selector plasmid (pCAS9-mCherry-Frame+2; Addgene_66941),[75] 2.5 μg target selector plasmid (pCS446_pSPgSMC3; this study) harboring SMC3 guide RNA (TGATACCACACATGGTTAATTGG), and 5 μg donor plasmid (pCS452_pCRISPaint-TurboID-pPGK-Hygro; this study). Cells were transfected with Fugene using standard procedures and subsequently selected using Hygromycin (Roche, Cat# 10843555001). Two single clones were isolated through serial dilution. PCR genotyping and sequencing verified monoallelic tagging. U2OS cell line expressing H2B-mNeon/mCherry-CENP-A and HeLa$^{EGFP\text{-}AID\text{-}Sororin}$ cell line expressing H2B-mNeon were obtained by lentiviral transduction (plasmids pLV-H2B-Neon-ires-Puro[77] and pLenti6-CENP-A-mCherry, Addgene_89767[78]) using standard procedures and subsequently FACS-sorted (single cells) based on mCherry and/or H2B-mNeon expression.

Stable transfection of DT40 cells was performed as described previously[82] to randomly integrate OsTIR1 into the genome of WTCDK1^{as} cell line[29] to create WTCDK1^{as}_TIR1 cell lines which was resistant to G418 1.5 mg/ml (Thermo fisher Scientific). TIR1 highly expressing clones were selected by western blotting using an antibody against TIR1 (a gift from Dr. Masato Kanemaki). SMC2-AID/CDK1^{as} cell line was described previously[31] and cultured continuously in the presence of doxycyline (0.5 μg/ml). In order to create SMC3-AID/CDK1^{as}, CAP-H-Halo/CDK1^{as}, Halo-CAP-H2/CDK1^{as} cell lines, we utilized Neon setting 24 (ThermoFisher Scientific). A rescue plasmid encoding mAID-Clover or Halo tag with resistance cassette flanked by ∼ 500 bp homologous arms (2 μg) and a plasmid encoding hCas9 and Guide RNA (6 μg) were transfected into 2-4 million cells suspended in 100 μl buffer R from the Neon kit. Hygromycin 0.8-1 mg/ml was used to select mAID-Clover or Halo tag integrated cell lines. A rescue plasmid to integrate Halo tag to the C-terminus (CAP-H) was constructed by Edinburgh Genome Foundry (University of Edinburgh). Rescue plasmids to integrate mAID-clover to the C-terminus of SMC3, Halo tag to the N-terminus (CAP-H2) or near the N-terminus (Cid) were constructed by Dr. Kumiko Samejima. Maps and DNA of those rescue plasmids and pX330 plasmids (Addgene_#158973)[76] encoding both hCas9/GuideRNA are available upon request to Dr Kumiko Samejima. After transfection of both rescue constructs and the pX330 plasmids, clones in which AID-clover or Halo tag were integrated all alleles are selected by western blotting and/or by genomic PCR analysis. Detailed protocols to establish DT40-AID/CDK1^{as} cell lines are available upon request to Dr. Kumiko Samejima. Halo-Cid Schneider cells were established at Prof Huen's laboratory.

Organoid culturing

PDO P9T H2B-GFP was cultured in medium containing advanced DMEM/F12 medium (Invitrogen), HEPES buffer (Sigma-Aldrich, 1 mM), penicillin/streptomycin (Sigma-Aldrich, 1%), Ala-Glu (Sigma-Aldrich, 0.2 mM), R-spondin-conditioned medium (20%), Noggin-conditioned medium (10%), B27 (Thermo/Life Technologies, 1×), nicotinamide (Sigma-Aldrich, 10 mM), N-acetylcysteine (Sigma-Aldrich, 1.25 mM), A83-01 (Tocris, 500 nM), EGF (Invitrogen/Life Technologies, 50 ng ml−1) and SB203580 (Invitrogen/Life Technologies, 3 μM). For passaging, PDOs were dissociated with TrypLE (Gibco) and replated in matrigel (Corning. 356231) in a pre-warmed 24-well plate. For immunofluorescence, monolayers of P9T were used. For that, coverslips in 24-well plates were coated with 150 μL of matrigel at a concentration of 0.8 mg/mL diluted in medium, followed by an incubation at 37°C for 2 hours. Organoids were dissociated and were washed once with media and resuspended in basal media supplemented with Rock inhibitor, Y-27632 (AbMole BioScience/Forlab, 10 μM). Approximately 300,000 cells were then seeded in a matrigel-coated coverslip. After 24 hours of culture, cells were transitioned to supplemented organoid media for the remainder of the experiment. Cells were synchronized overnight with RO-3306 and released with three washes of fresh media. Pre-extraction and fixation were performed 1.5 hours after the RO-3306 release, following the same steps detailed in the immunofluorescence section.

Treatments on human cells

Where indicated, cells were arrested in G_2 by the addition of RO-3306 (10 μM; Tocris Bioscience, Cat# 4181) and released with three washouts in fresh media. For Aurora B inhibitions, ZM-447439 (2 μM; Tocris Bioscience, Cat# 2458) and MG-132 (5 mM; Sigma-Aldrich, Cat# C2211) were added 20 minutes after the RO-3306 release, and fixed 40 mins later. Thymidine synchronization was performed for 24 hours and cells were released with three washouts in fresh media, or in the presence of drugs, as indicated. In Sororin

depletions, 3-indoleacetic acid (IAA) (500 μM; Sigma-Aldrich, Cat# I5148-2G) was added overnight together with RO-3306, or just after the thymidine release, and maintained in all the subsequent steps. In SMC2 depletions, HCT-116$^{AID\text{-}mCherry\text{-}SMC2}$ were synchronize with thymidine and supplemented with doxycycline (1 μg/ml; Sigma-Aldrich, Cat# D9891) to induce the expression of OsTIR1. After 24 hours, cells were released in fresh media containing IAA and nocodazole (3.3 μM; Sigma-Aldrich, Cat# M1404), where specified. Monastrol (200 μM; Tocris Bioscience, Cat# 1305) was added to unsynchronized HeLa cells for 3 hours, followed by release with three washouts in fresh media, and fixed 1.5 hours later. In TurboID experiments, Biotin (500 μM,Sigma-Aldrich; Cat# B4501-5G) was added to the media 30 minutes before fixation.

siRNA transfection

For knockdown experiments, 100 nM of siRNA were transfected (siGAPDH (Dharmacon, D-001830-01-05), siRAD21 (SMARTpool: ON-TARGET plus Dharmacon L-006832-00-0010), siKif18A (5'CCAACAACAGUGCCAUAAAUU3'; Dharmacon custom[73]) siWAPL (5' GAGAGAUGUUUACGAGUUU 3', Dharmacon J-026287-10)). RPE-1 cells were transfected with Lipofectamine RNAi Max (Thermo Fisher Scientific) according to manufacturer's instructions and fixed 48 hours later. Hela cells were transfected using Hiperfect (Qiagen) according to manufacturer's instructions. A second transfection was conducted after 12 hours. 8 hours after the second transfection, cells were synchronized with RO-3306 overnight. Following synchronization, cells were released into fresh media and fixed one hour later.

Plasmid construction

The list of primers used in this study can be found in the key resources table. The gRNAs for SMC3 was cloned into the vector pSPgRNA (Addgene_47108)[74] using primers H567/H568, as described previously.[83] pCS452_pCRISPaint-TurboID-pPGK-Hygro was created by Gibson cloning in two steps. First, TurboID contruct derived from 3xHA-TurboID-NLS_pCDNA3 (Addgene_10717)[49] was cloned into the BamHI site of plasmid CRISPaint-mNeon (addgene_174092)[75] with primers H574/H575 to create pCS451_CRISPaint-TurboID-mNeon. Next, mNeon was substituted with pPGK-Hygro derived from pMK290 (Addgene_72828)[84] using primers H582-H585.

Immunofluorescence

For immunofluorescence, cells grown on 12 mm coverslip (no. 1.5H) were permeabilized for 1 min with 0.1 M PHEM buffer (60 mM PIPES, 25 mM HEPES, 2 mM $MgCl_2$, 10 mM EGTA, pH 6.9) with 0.5% Triton-X-100, followed by fixation for 10 min with 4% PFA (Electron microscopy sciences, Cat# 15710) in PBS. Both pre-extraction and fixation solution were pre-warmed to 37 °C. For analysis of cold-stable microtubules, cells were placed for 5 min on ice water prior to pre-extraction and fixation. After fixation, coverslips were washed three times with PBS and blocked with 3% BSA in PBS for 1h at room temperature. For Hec1 immunostaining, samples were blocked for another hour in 3% milk in PBS. Primary antibodies diluted at 1:100 in 3% BSA, or in 1.5%BSA/1.5%milk for the case of Hec1 antibody, were added to the coverslips and incubated for 4 hours at RT (a list with the primary[66] and secondary antibodies can be found in the key resources table). Subsequently, cells were washed three times with 0.5 % triton in PBS and incubated with DAPI (1 μg/mL) and secondary antibodies diluted 1:100 in 3% BSA for another 2 hours at RT. Next, coverslips were washed three times with 0.1% Triton and prepared for ExM or mounted onto glass slides using Prolong Gold antifade.

OVSAHO cells were pre-extracted with 1 mL of cytoskeleton extraction buffer solution (0.1 M PIPES, 1 mM MgCl2, 1 mM EGTA, 0.5% Triton-X-100, pH=7.0) for 20 seconds. Subsequently, the cells were fixed in a solution containing 3% paraformaldehyde (BioGnost, Cat# F4-1L) and 0.05% glutaraldehyde (Sigma, Cat# G7651) for 10 minutes. Both pre-extraction and fixation solution were pre-warmed to 37 °C. Following fixation, a quenching solution (100 mM glycine in PBS, Milipore, Cat# 104201) and a reduction solution (0.1% sodium borohydride in PBS, Sigma, Cat# 452882) were added for 7 and 10 minutes, respectively. The cells were then treated with 0.5% Triton-X-100 (Sigma, Cat# 93426) for 15 minutes. Samples were incubated at room temperature in blocking buffer (2% normal goat serum, Thermo Fisher Scientific, Cat# 10000C, RRID: AB_2532979). Microtubules were then labeled using a rat anti-alpha-tubulin monoclonal primary antibody solution (diluted 1:250 in blocking buffer, Thermo Fisher Scientific, Cat# MA1-80017, RRID: AB_2210201), and centromeres with human anti-centromere proteins primary antibody solution (ACA, diluted 1:500 in blocking buffer, Antibodies Incorporated, Cat# 15-234, RRID: AB_2939058), with an overnight incubation at 4 °C. After washing with PBS, secondary antibodies, Donkey Anti-Rat IgG H&L Alexa Fluor® 594 (dilution 1:500, Abcam, Cat# ab150156, RRID: AB_2890252) and Goat polyclonal Antibody to Human IgG H&L DyLight488 (dilution 1:500, Abcam, Cat# ab96907, RRID: AB_10680094) were applied and incubated for 1 hour at room temperature. Finally, following a PBS wash, DAPI solution (1 μg/mL, Sigma, Cat# D9542) was applied and incubated for 15 minutes at room temperature to visualize chromosomes.

Expansion Microscopy (ExM)

For ExM,[27] stained samples were treated with 0.1 mg/ml Acryloyl-X (Thermo Fisher A20770) in PBS for 2 hours, washed three times with PBS and incubated for 5 min in monomer solution (1×PBS, 2M NaCl, 2.5% (wt/wt) acrylamide 0.15% (wt/wt) N,N'-methylene-bisacrylamide 8.625% (wt/wt) sodium acrylate). Coverslips were placed on top of a drop of 90 μl of freshly prepared gelation solution (monomer solution supplemented with 0.2% (wt/wt) TEMED and 0.2% (wt/wt) APS) and incubated for 1 hour at 37 °C. Gels were then incubated in digestion solution (8 units/ml proteinase K, 1×TAE, 0.5% TX-100, 0.8M guanidine HCl) for 2 hours at 37 °C and washed in PBS containing DAPI (1 μg/mL). For partial ExM (Figures 6D and S7A), gel was washed several times with PBS (2-fold expansion).

Full expansion was performed in a 10-cm plate by several washings of 30 minutes with excess volume of Milli-Q water (4-4.5-fold expansion). Expanded samples were immobilized on 25 mm (No. 1.5H) coverslips covered with 0.01 % (w/v) poly-L-lysin (Sigma-Aldrich, Cat# P8920) and imaged.

Microscopy and image processing

Images from Figures 1F, 1G, 3A, 4A, 4B, 5D, 6G, 7F, S3A, and S3C were acquired on a deconvolution System (DeltaVision Elite Applied Precision/GE Healthcare) with a ×100/1.40-NA objective (Olympus) using SoftWorx 6.0 software (Applied Precision/GE Healthcare). Images were acquired as z-stacks at 0.2 μm intervals and deconvolved using SoftWoRx. Images from Figures 1A, 1H, 1I, 7E, S1A, S1B, S1E, S1J, and S7D were acquired on a a Nikon Ti-E motorized microscope equipped with a Zyla 4.2Mpx sCMOS camera (Andor) and 100×1.35-NA objective lens (Nikon). Images were acquired as z-stacks at 0.2 μm intervals. Images from Figures 3H, 6D, 6I, S6E, and S7A were acquired on a Zeiss LSM900 Airyscan2 with a 63x1.3-NA and using the Multiplex SR-2Y mode. For each experiment, optimized sectioning calculated by Zeiss software was used. iSIM images were acquired on a Nikon Ti2-E Microscope equipped with a VT-iSIM Super Resolution unit (VisiTech), a Prime BSI Express sCMOS camera (Photometrix) and a TIRF 100x1.49-NA objective lens (Nikon). Images were acquired as z-stacks at 0.5 μm intervals in live-cell imaging and 0.1 or 0.2 μm intervals in fixed samples. Images from Nikon and Zeiss systems were deconvolved with Huygens Professional (v20.10) using up to 40 iterations of the Classic Maximum Likelihood Estimation (CLME) algorithm with theoretical PSF. 3D reconstructions were created with Imaris Software (v9.7.2) (Bitplane). Confocal and Stimulated Emission Depletion Microscopy (STED) images of HCT-116 cells were taken with an Abberior Instruments STEDYCON STED setup equipped with an inverted IX83 microscope (Olympus), an APO100x1.4-NA oil objective and a pulsed 775 nm STED depletion laser. Star Orange was imaged with a pixel size of 25 nm and a pixel dwell time of 10 μs. The 640 (29% laser power) nm laser line was used for excitation, and the 775 (100% laser power) nm laser line was used. All acquisition operations were controlled by the STEDYCON Software (Abberior Instruments). by Bitplane. STED images of OVSAHO cells were filmed using an Expert Line easy3D STED microscope system (Abberior Instruments) with the 100 x/1.4NA UPLSAPO100x oil objective (Olympus) and an avalanche photodiode detector (APD). Super-resolution images were acquired for the Alexa Fluor® 594-tubulin signal, while the DyLight488 and DAPI signals of kinetochores and chromosomes, respectively, were captured at confocal resolution. The 561 (40% laser power), 488 (20% laser power), and 405 (1% laser power) nm laser lines were used for excitation, and the 775 (40% laser power) nm laser line was used for depletion during STED super-resolution imaging. The images were acquired using Imspector software. The xy pixel size for fixed cells was set to 20 nm and 10 focal planes were acquired with a 300 nm distance between the planes. The 405 channel was separately taken immediately after the simultaneous acquisition of 488 and 561 channels within the same imaging region. STED images of HeLa cells were taken using a Leica Stellaris 8 setup, equipped with a pulsed white-light laser, HyD detectors and a HC PL APO CS2 100x/1.40 OIL objective. Scanning was done at 100 Hz, with a pinhole setting of 1 AU (at 580 nm), and a pixel size set to 16 × 16 nm. Optimized sectioning calculated by Leica software was used. For Abberior STAR Red (Cat) a 637 nm laser line (2% laser power) for excitation and a 775 nm synchronized pulsed laser for depletion (50% laser power). For Streptavidin-Alexa 488, confocal imaging was done with a 499 nm laser line (2% laser power). The signals were detected with Hybrid detectors with the following spectral settings: Streptavidin-Alexa488 (emission 504–585; gain 0, intensity mode), Abberior STAR Red (emission 646-829; gain 200, intensity mode). For quantifications and visualization, CENP-A STED images were smoothened by applying a Gaussian filter of 0.015 μm using Imaris Software (v9.7.2) The rest of images presented in the figures were only adjusted in brightness and contrast on raw or deconvoluted data using the Fiji software.

Live-cell imaging

For live-cell imaging, cells were seeded in 24-well glass bottom plates (No. 1.5H) (Cellvis, P24-1.5H-N). High-resolution live-cell imaging of U2OS$^{mCherry\text{-}CENP\text{-}A/H2B\text{-}mNeon}$ cells was performed over 16 z-slices separated by 500 nm every 10 seconds on a Nikon Ti2-E Microscope equipped with a VT-iSIM Super Resolution unit (see above). Images were deconvolved with Huygens Professional (v20.10) using the conservative profile.

Live STED images were filmed at the Core Facility Bioimaging at the Biomedical Center, LMU Munich, as described previously.[85] Super-resolution images were acquired for the SiR-tubulin signal, while the GFP signal of kinetochores was acquired at confocal resolution. Gated STED images were acquired with a Leica TCS SP8 STED 3X microscope with pulsed white light laser excitation at 652 nm and pulsed depletion with a 775 nm laser (Leica). The used objective was HC PL APO CS2 ×93/1.30NA GLYC with a motorized correction collar set to 63%. Scanning was done at 30 Hz, with a pinhole setting of 0.93 AU (at 580 nm), and a pixel size set to 33.29 × 33.29 nm. The signals were detected with Hybrid detectors with the following spectral settings: SiR-tubulin (excitation 652; emission: 662–692 nm; counting mode, gating: 0.35–6 ns) and GFP (excitation 488; emission 498–550; counting mode, gating: 0.50-6 ns). The STED 775 nm laser was delayed by -150 ps. Cells were stained with SiR-tubulin dye (Spirochrome AG, Cat# CY-SC002) at 100 nM concentration, 1 h before imaging.

Stretched chromosomes

Cells were seeded in 6-well plates at 50% confluency and incubated in 2 mM thymidine for 24 hours and released in 3.3 μM nocodazole overnight. In the morning, cells were harvested by mitotic shake-off, washed with PBS and resuspended in 15 ml of pre-warmed 0.4% Citrate solution. Cells were then incubated at 37°C for 20 mins and a 500 ml aliquot was cytospun (1200 rpm for 10 min at high acceleration) onto coated slides (Thermoscientific; 5991055). Cells were fixed in 4% PFA and immunostained.

Please cite this article in press as: Sacristan et al., Vertebrate centromeres in mitosis are functionally bipartite structures stabilized by cohesin, Cell (2024), https://doi.org/10.1016/j.cell.2024.04.014

Immunofluorescence Image analysis

ImageJ (https://imagej.nih.gov/ij/)/Fiji (http://fiji.sc/#) (National Institute of Health) plot profile tool was used to measure intensity profiles, and intensities were normalized between 0 and 1. Quantification of number of centromere subdomains and k-fibers were manually scored in z-stacks using Fiji.

Distance between CENP-A subdomains in ExM and STED images was measured with Imaris Software (v9.7.2) (Bitplane). For that, individual subdomains were detected using the spot detection tool set to an estimated XY diameter of 150 nm for ExM images. For STED images, CENP-A signal was first smoothened by applying a Gaussian filter of 0.015 μm. Subsequently subdomains were segmented with the spot detection tool set to an XY diameter of 80 nm and the Z diameter to 180 nm. The distance between the center of detected spots was measured with the measurement point tool. To minimize the error derived from axial chromatic aberration, only centromeres with subdomains that shared the same approximate focal plane were used for quantification.

Quantifications of merotelic attachments were done using Imaris Software (v9.7.2) (Bitplane). Single kinetochores were segmented based on the CENP-C signal using the spot detection tool set to an estimated XY diameter of 300 nm. To identify kinetochores with stretched subdomains, the Hec1 signal was segmented by using the spot detection function with XY set at 175 nm and spots were selected based on a proximity closer to 300 nm with respect to the nearest CENP-C spot. Kinetochores with a single Hec1 spot were filtered out by applying a closest neighbor filter of 500 nm. This threshold was determined under ZM-447439 conditions, where larger distances did not increase the number of detected subdomains but resulted in a higher incidence of false positives from close kinetochores. In contrast, due to the severe separation of subdomains in Sororin depletions, the closest neighbor filter was empirically set to 800 nm. Finally, merotelics were manually curated based on the orientation of the two subdomains, counting only those subdomains facing opposite poles. To identify non-stretched Hec1 subdomains a spot size of 80 nm and a distance to the closest CENP-C spot of 300 nm was used. Then, mono-oriented Hec1 subdomains were manually curated. The distance between the centers of Hec1 spots within the same kinetochore was measured using the measurement point tool. CENP-B and CENP-C signals were used to visually verify that Hec1 spots belonged to a single kinetochore.

SMC3 intensities were measured with Imaris Software (v9.7.2) (Bitplane). For that, CENP-C (kinetochores) and Sgo2 (inner centromere) were identified with the spot detection tool with an XY diameter set to 800 nm. To exclude the kinetochore pool of Sgo2, spots closer than 400 nm to other CENP-C spots were filtered out. Background was determined within the DAPI signal in regions devoid of centromeres. Subsequently, the mean intensity of SMC3 within CENP-C and Sgo1 spots was calculated and subtracted from the mean signal of the background. Individual SMC3 values were then normalized to the mean intensity of SMC3 within the kinetochores of the positive control treated with biotin.

Analysis of electron tomography images

To estimate the number and split position of a k-fiber bundle at the kinetochore we perform statistical analysis. From each k-fiber, we extract 3D coordinates of all plus-ends and we computed the standardized Euclidean distance between two n-vectors *i* and *j*. Where *i* is in-going and *j* is out-going plus-end coordinate. This allows to obtain a 2D matrix feature representation of plus-ends that is used to generate a fully connected graph of all points (Figure S3E). The graph is a diagram data representation that contains nodes (plus-ends) and edges (relationships between two connected plus-ends). The edges are represented by the distance between connected plus-ends. To simplify this, point distances were normalized with an exponential function (Figure S3E), which allows to standardize distances using pixel size value and normalize all distances between 0 and 1. Normalized values were used as the probability that the edges between connected points are true or false, and performed a normalized graph cut. This allowed to determine which k-fibers are split at the kinetochore purely based on distances between plus-ends. We then compared the mean values of the k-fiber doublets fraction between all three HeLa cells obtained from the Kiewisz et al.[34] dataset. To compute the distance between split k-fiber centers, we measured the center of each identified fiber's mass and the Euclidian distance between them.

CENP-A ChIP-seq experiments and analysis

Nuclei were isolated from 1.5×10^9 DT40 cells and digested with 60 units/ml MNase (Takara Bio Inc.) in buffer A (15 mM Hepes-KOH, pH 7.4, 15 mM NaCl, 60 mM KCl, 1 mM CaCl2, 0.34 M sucrose, 0.5 mM spermidine, 0.15 mM spermine, 1 mM DTT, and 1× complete protease inhibitor cocktail; Roche). After centrifugation at 17,800 g for 5 min, the chromatin pellet was suspended with buffer B (20 mM Tris-HCl, pH 8.0, 0.5 M NaCl, 10 mM EDTA, and 1× complete protease inhibitor cocktail; Roche), and then mononucleosome was extracted. The extracted mononucleosome fraction was incubated for 2 h at 4°C with Protein G Sepharose beads (GE Healthcare), which were preincubated with rabbit polyclonal anti–chicken CENP-A antibody.[67] Beads were washed with buffer B four times, and the bound DNA was purified by phenol-chloroform extraction and ethanol precipitation. The purified DNA was analyzed on a DNA sequencer (HiSeq 2500; Illumina). ChIP-seq libraries were constructed with the TruSeq DNA LT Sample Prep kit (Illumina) as described in the protocols provided with the kit. In brief, ~50 ng of purified DNA was end-repaired, followed by the addition of a single adenosine nucleotide at 3' and ligation to the universal library adapters. DNA was amplified by eight PCR cycles, and the DNA libraries were prepared. ChIP DNA libraries were sequenced using the HiSeq 2500 in up to 2 × 151 cycles. Image analysis and base calling were performed with the standard pipeline version RTA1.17.21.3 (Illumina).

Single-end reads (100bp) were trimmed with Trimmomatic v0.36[79] to remove adapters and low-quality bases. Trimmed reads were aligned to the galGal7 reference genome using BWA mem v0.7.16 and unique alignments were selected for downstream analysis. Read coverage profiles were generated with deepTools bamCoverage v3.5 using bins per million mapped reads (BPM) normalisation.

HALO ChIP-seq experiments and analysis

CAP-H-Halo/CDK1^{as} or Halo-CAP-H2/CDK1^{as} DT40 cells were treated with 2μM 1NMPP1 for 13h to block the cells at G_2. After washout of 1NMPP1, cells were released into new media, then collected at 5 min (prophase), 7.5 min (early prometaphase), and 30 min (late prometaphase). Each sample was prepared from 10 million Chicken DT40 cells and 4 million Drosophila melanogaster S2-CID-Halo cells. Those cells were fixed separately with 1% formaldehyde for 10 minutes at room temperature under shacking condition. Fixed cells were then quenched with freshly prepared 1.25 M glycine for 5 minutes at room temperature on a shaker and washed with ice-cold PBS for three times. The cells were then snap-frozen using dry ice and ethanol and preserved at -80℃ for ChIP-Seq. Briefly, DT40 and S2-CID-Halo cell pellets were thawed on ice and mixed together. The cells were then lysed with 110 μl of cold lysis buffe (1% SDS, 10 mM EDTA, 50 mM Tris-HCl (pH 8.1), 0.1 mM DTT, and protease inhibitor cocktail) by incubating for 14 minutes on ice. Subsequently, 440 μl of IP dilution buffer (1% Triton X-100, 2 mM EDTA, 20 mM Tris-HCl (pH 8.1), 150 mM NaCl, 0.1 mM DTT, and protease inhibitor cocktail) was added. To shear the genomic DNA, cell lysates were then sonicated for 14 cycles (30 sec on/off) at maximum power using Bioruptor® Plus sonication device. After centrifugation to remove debris, Triton X-100 was added to the lysates to achieve a final concentration of 1% for IP. Ten percent of sheared chromatin was set aside for Input, and the rest was incubated with equilibrated Halo-Trap Agarose beads (ChromoTek) for overnight at 4℃ on a rotating wheel. The beads were washed 2 times for 10 minutes at 4℃ with three different wash buffers: wash buffer 1(1% Triton X-100, 2 mM EDTA, 20 mM Tris-HCl (pH 8.1), 150 mM NaCl, 0.1 mM DTT and protease inhibitor cocktail), wash buffer 2 (50 mM Hepes pH 7.9, 1% Triton X-100, 1 mM EDTA, 50 mM Tris-HCl (pH 8.1), 500 mM NaCl, 0.1% Na-deoxycholate, 0.1% SDS, 0.1 mM DTT and protease inhibitor cocktail), wash buffer 3 (20 mM Tris-HCl pH 8.0, 1 mM EDTA, 250 mM LiCl, 1% NP-40, 0.1% Na-deoxycholate, 0.1 mM DTT and protease inhibitor cocktail). Finally, beads were washed with TE buffer (1 mM EDTA, 10 mM Tris-HCl pH 8.0) twice, and chromatin were extracted by incubating the bead with extraction buffer (0.1 M $NaHCO_3$, 1% SDS) twice at 65℃ on a thermomixer for 15 mins. To reverse cross-linking, IP-DNA and Input-DNA were incubated with 200 mM NaCl at 65℃ overnight. Then, they were treated with RNase-A at 37℃ for 1 hour and then with proteinase K at 65℃ overnight. DNA was purified by using the QIAquick PCR Purification Kit. After quantification with the Qubit assay, ChIP-Seq libraries were prepared using the NEBNext® Ultra™ II DNA Library Prep Kit for Illumina® with NEBNext® Multiplex Oligos for Illumina® (Index Primers Set 1) according to the manufacturer's protocol. The library size distribution was analysed by Agilent Bioanalyzer with High Sensitivity DNA chip and submitted for Illumina deep sequencing at the Edinburgh Clinical Research Facility. Sequencing (2x50) was performed on the NextSeq 2000 platform using the NextSeq 1000/2000 P^2 Reagents (100 cycles) v3 Kit. ChIP-seq datasets were processed using a custom built Snakemake pipeline. 51bp paired end reads were trimmed with Cutadapt v1.18 to remove adapters and low quality sequence with the parameters –minimum-length 20 –nextseq-trim=20. Trimmed reads were aligned to the galGal7b reference genome with BWA mem v0.7.16 and the output was filtered for primary alignments. Read coverage profiles were generated with Deeptools v3.50 bamCoverage using a bin size of 1b and BPM (bins per million) normalisation. Read profiles relative to the Input samples were generated with Deeptools v3.50 bamCompare using a bin size of 20b and BPM normalisation to calculate a $\log_2$ ratio.

In order to calculate the enrichment score of condensins at Z cen/5cen compared to those at the corresponding chromosomes (Figure S6C), the read counts of condensin I (CAP-H-Halo) and II (Halo-CAP-H2) were normalized using the input data for the Z or 5 centromere region (25 kb each) and for the entire Z or 5 chromosomes (86 Mb and 59 Mb, respectively). Subsequently, the frequency of condensin I and II at the centromere and the whole chromosome (number/kb) was calculated. The enrichment score of condensin I and II at the centromere was determined by dividing the frequency of condensins at the centromere by those at the chromosome.

Capture-C experiment and analysis

Careful analysis in DT40 cells reveals that the size of the core centromere remains mostly constant but the centromere position can drift over time in culture. (Importantly, it does not shift for any significant distance in cultures grown for <2 weeks grown from a single cell). Therefore, we performed CENP-A ChIP-seq to define the position of core centromeres in each subclone of wt/CDK1^{as}, SMC2-AID/CDK1^{as} and SMC3-AID/CDK1^{as} cell lines. The Zcen position in the wt and SMC2-AID subclones was similar (43,367-43,392 kb and 43,367-43,395 kb respectively, based on the Galgal7 genome annotation (Figure S2B)). In our SMC3-AID/CDK1^{as} subclone the centromere position had shifted towards the q arm side by ~10 kb (43,379-43,405 kb). Based on this mapping, we designed 34 viewpoints spaced 5-6 kb apart, covering 217 kb surrounding the ~30 kb CENP-A region at the core of the Zcen (Figure S2B; Table S3). Two chromosome 5 in wt subclones have 5cen at different positions, according to our CENP-A ChIP seq data (Figure S2C). Our SMC2-AID/CDK1^{as} subclone shows a broader peak of CENP-A suggesting cen5 positions are also not same in this subclone. Our SMC3-AID/CDK1^{as} subclone shows ~30 kb peak, suggesting the two centromere positions are similar. Based on this mapping, we designed 27 viewpoints spaced 5-6 kb apart, covering 254 kb surrounding the ~30 kb CENP-A region at the core of the 5cen (Figure S2C; Table S3). Each viewpoint corresponds to a DpnII-digested fragment with 2 capture-oligos complementary to either end of the fragment. To avoid the effect of non-cleaved restriction sites, 1-3 kb surrounding each fragment cannot be used for the interaction map. Therefore, the oligos were split into 3 pools (A, B, C) for Zcen and 2 pools (D, E) for 5cen to space the fragments

further apart. In order to follow structural change of centromeric chromatin upon mitotic entry, typically 30 million cells were used for each sample. CDK1^{as} cells were treated with 1NMPP1 (13 h) to arrest cultures in late G_2. Auxin (final concentration 125-150 μM) were added to the culture for the final 3h during the 1NMPP1 treatment to deplete SMC2 or SMC3 from SMC2-AID/CDK1^{as} or SMC3-AID/CDK1^{as} cells, respectively. Mitotic cells (late prometaphase cells) were obtained from the culture incubated for further 30 min (SMC3-AID) or 45 min (SMC2-AID) after 1NMPP1 washout. In order to determine the effects of the mitotic spindle on kinetochores, 0.5 μg/ml nocodazole was added after 1NMPP1 washout (sample = Mnoc). G_2 or mitotic cells were cross-linked with 16% formaldehyde solution (final concentration 1%) in culture media for 10 minutes at room temperature, then 2.5 M glycine (final concentration 124 mM) was added to stop crosslinking for 5 minutes at room temperature and then on ice for at least 15 min. Those cells collected by centrifugation (2000 g for 5 min) and washed once with PBS. The cell pellets were frozen in dry ice and kept in -80C. Essentially, we followed the published protocol (https://doi.org/10.1038/nmeth.3664). Briefly, cells were lysed with 3C lysis buffer (10 mM Tris-HCl (pH 8), 10 mM NaCl, 0.2% igepal, EDTA free protease inhibitor), and super natant was removed after centrifugation. Cell pellet was further lysed with 0.5 % SDS in H_2O. Cell lysate was digested with DpnII in the presence of Triton X-100 (final conc 1.6%). Digested DNA in the lysate was ligated and then treated with proteinase K and RNAseA/T1DNA cocktail. The lysate was treated with Phenol/chloroform/isoamyl alcohol and the DNA was extracted by addition of sodium acetate and ethanol (3C DNA). Using these 3C DNA, 3C libraries were constructed using NEBNext Ultra II DNA library prep kit and index oligo pool 1 and 2 for Illumina following the manufacture's instruction. Those 3C libraries (1.5 μg DNA each) were subjected to double hybridization with biotinylated capture oligo pools to enrich the fragments of interest. 1st hybridization was performed at 47C for 72 h. DNA fragments bound to the capture oligos were collected with streptavidin beads following NimbleGen SeqCap EZ SR user's guide 4.0, and amplified with NEBNext UltraQ5 Master Mix. With the amplified DNA fragment (1 μg each), 2nd 1st hybridization was performed at 47C for 24 h. After subsequent clean-up with streptavidin beads and amplification, the resultant Capture-C libraries were subjected to illumina sequencing (150 bp paired read). The sequencing data was analysed with the capC-MAP software.[81] Two biological replicates (using different starting cell pellets) were performed for each condition.Click or tap here to enter text.

Polymer physics modelling

For the polymer physics modelling, coarse-grained molecular dynamics simulations were performed, in which collections of molecules are represented by beads, which interact with phenomenological force fields and move according to Newton's laws.[86] More specifically, chromatin fibres and chromosomes were modelled as bead-and-spring polymers, while bridging proteins representing, for instance, condensin or cohesin complexes were represented by additional individual beads. We used the multi-purpose molecular dynamics package LAMMPS (Large-scale Atomic/Molecular Massively Parallel Simulator[80]). In this section we detail the potentials underlying the force fields used in the simulations.

The chromatin fibre

A chromatin fibre, corresponding to a 440 kbp chromatin region surrounding the core centromere, was discretised as a set of monomers, each of size corresponding to 1 kbp, or to a physical size $\sigma \sim$ 10-20 nm, which could in principle be determined by fitting to microscopy experiments. There were three types of chromatin beads: one representing pericentromeric chromatin (PC), one representing the middle of the core centromere (CM, 11 kbp in total, see below) and one representing loop bases (LB) in PC. Below we specify when the potentials used depend on chromatin bead type. When nothing is specified, the potential is applied regardless of bead type.

Any two monomers (*i* and *j*) in the chromatin fibre interact purely repulsively, via a Weeks-Chandler-Anderson (WCA) potential, given by

$$U_{ij}^{\mathrm{WCA}}(r_{ij}) = \begin{cases} 4k_BT\left[\left(\frac{\sigma}{r_{ij}}\right)^{12} - \left(\frac{\sigma}{r_{ij}}\right)^{6} + \frac{1}{4}\right] & \text{if } r_{ij} < 2^{1/6}\sigma \\ 0 & \text{otherwise,} \end{cases} \quad \text{(Equation 1)}$$

where r_{ij} is the separation of beads *i* and *j*. There is also a harmonic elastic spring acting between consecutive beads in the chain to enforce chain connectivity. This is given by

$$U_{ij}^{harm}(r_{ij}) = k_{\mathrm{harm}}(r_{ij} - r_0)^2, \quad \text{(Equation 2)}$$

where *i* and *j* are neighbouring beads, $r_0 = 1.1\sigma$ is the maximum separation between the beads, and $k_{harm} = 100k_BT/\sigma^2$ is the spring constant. Additionally, a triplet of neighbouring beads in the chromatin fibre interacts via a Kratky-Porod term to model the stiffness of the chromatin fibre, which explicitly reads as follows,

$$U_{ij}^{\mathrm{KP}} = \frac{k_BTl_p}{\sigma}[1 - \cos\theta_{ij}], \quad \text{(Equation 3)}$$

where *i* and *j* are neighbouring beads, while θ_{ij} denotes the angle between the vector connecting beads *i* and *j* = *i+1* and the vector connecting beads *j* and *j+1*. The quantity l_p is related to the persistent length of the chain. We set it to 3σ in our simulation for adjacent beads, which corresponds to a relatively flexible chain. For model 3, we set this value to 10σ for beads in the CM, which means that the latter region is locally stiffer in those simulations.

Please cite this article in press as: Sacristan et al., Vertebrate centromeres in mitosis are functionally bipartite structures stabilized by cohesin, Cell (2024), https://doi.org/10.1016/j.cell.2024.04.014

Chromatin bridges

An important component of the model is constituted by multivalent chromatin-binding proteins, or bridges, which can bind to chromatin at multiple places. Chromatin bridges were modelled as spheres, again with size σ for simplicity. While these may represent a number of factors, we identified the two bridges simulated with condensin and cohesin (see main text). This is motivated by recent work showing that SMC proteins have a bridging activity alongside a chromatin looping (or extrusion) activity.[44]

In our simulations, the interaction between a chromatin bead, a, and a multivalent chromatin bridge, b, was modelled via a truncated and shifted Lennard-Jones potential, given by

$$U_{ab}^{\mathrm{LJ}}(d_{ab}) = \begin{cases} 4\epsilon_{ab}\left[\left(\frac{\sigma}{d_{ab}}\right)^{12} - \left(\frac{\sigma}{d_{ab}}\right)^{6} - \left(\frac{\sigma}{r_c}\right)^{12} + \left(\frac{\sigma}{r_c}\right)^{6}\right] & \text{if } d_{ab} < r_c \\ 0 \text{ otherwise,} \end{cases} \quad \text{(Equation 4)}$$

where d_{ab} denotes the distance between the centres of the chromatin bead and protein, $r_c = 1.8\,\sigma$ is a cut-off parameter, and ϵ_{ab} determines the interaction strength between the bridge and chromatin. Note this is not equal to the value of the potential at the minimum point in view of the shift. The values of ϵ_{ab} chosen are discussed below (see parameter values and details of specific models). When bridges did not stick to a given chromatin region, the corresponding potential was instead set to a WCA potential as in Equation 1, corresponding to only steric interactions. Bridges also interacted with each other via steric interaction only (WCA potential).

Bridges could switch back and forward between a binding and a non-binding state with a rate k_{sw}. This feature mimics post-translational modifications on protein complexes and accounts for the dynamical turnover of constituents within nuclear protein clusters[45] When bridges were non-binding, they interacted with chromatin beads via the WCA potential.

Parameter values and details of specific models

While general parameter values used in all simulations are mentioned above, here we list the model-specific parameters we used.

The values of ϵ_{ab} chosen for each case as given in Table S2 (in units of k_BT). In Model 0, we considered a single bridge (representing condensin, or Multivalent Protein 1 (MP1) in the main text), which could bind to PC more weakly than to the CM. This resulted in an "inverted" Capture-C signal with respect to our mitotic one, and to a compact configuration with the CM being internal. In Model 1, we consider two bridges, with condensin binding more strongly to PC than to the CM. This led to a qualitatively correct Capture C signal, and to a switch in the CM location, which was now peripheral. In Model 0 and 1, no switching was considered. In Model 2, we used parameters as in Model 1, but both bridges could switch at a rate $k_{sw} = 0.001\ \tau_B^{-1}$, where the Brownian time $\tau_B = \sigma^2/D$, with D the diffusion coefficient of the beads. The Brownian time gives an order-of-estimate measure of the time it takes for a bead to diffuse across its own diameter, and it is this timescale which one can use to determine the mapping of simulation time to real time where required.

In Model 3, we also included chromatin loops, mimicking the looping activity of SMC proteins (and arising for instance due to loop extrusion and important for mitotic chromatin formation.[31,46] We included for simplicity fixed chromatin loops. Chromatin loops in a simulation were distributed randomly in PC, according to a Poisson distribution with average loop size equal to 40 kbp. We simulated over a number of runs (typically 50 for each condition), and each run was performed with a different set of random loops. For these runs, the two loop bases corresponding to each chromatin loop interacted with a harmonic spring, Equation 2, with $r_0 = 1.8\sigma$ and $k_{harm} = 100 k_BT/\sigma^2$. These loops create a bottlebrush topology. To control the stiffness of the backbone of the bottlebrush (consisting in the bases of consecutive loops), we included a Kratky-Porod potential, Equation 3, between consecutive LB beads, with $l_p = 10\sigma$. Regarding bridges, when modelling mitotic conditions, we considered two cases. In the first, we only included condensin-like bridges, which could bind strongly to LBs in PC, moderately to other PC beads, and weakly to the CM (Figures 5A and 5B, MP1 of the main text). We also performed additional simulations including cohesin (or MP2 in the main text), modelled as an additional bridge with moderate interactions to PC and stronger affinity for the CM. To represent G_2 conditions, we modelled cohesin activity as a strong interaction with the CM and for simplicity we neglected interactions between condensin and CM and between cohesin and PC. In model 3, we considered switching bridges with rate $k_{sw} = 0.001\ \tau_B^{-1}$. The only exception was the G_2 condition, where the cohesin-like bridge did not switch.

Numbers of bridges were chosen as follows: 100 (condensin) in model 0, 100 (condensin) in model 1, 200 (condensin) in model 2, 100+100 (condensin+cohesin) in model 3. When switching was included, half of the bridges of any type were active on average at any given time.

In model 3, we found a transition, or crossover, between a mitotic-like state (M) and an interphase-like state (G_2). The former has typically a bipartite structure with condensin-rich clusters separated by a largely unstructured CM. In the latter, cohesin forms an additional cluster at the CM. The transition between the M and the G_2-state can be triggered, for instance, by increasing the affinity between the cohesin-like bridge and the CM.

Additional simulation details

To simulate Capture-C directionality curves, we identified contacts made by each chromatin bead (say bead i) with all other beads j. Two beads were considered to be in contact if their 3D distance was below a cross-linking threshold, which was varied for each condition to fit the experimental data (with the exception of model 0, which is not qualitatively right so that fitting is not possible). From contact data, directionality curves were drawn by computing for each bead i the natural logarithm of the ratio between the interactions in the region to the left of i and the interactions to the right of i. For both right and left interactions, contacts were summed up

between a lower and an upper end threshold, equal to 3 kbp and 100 kbp respectively. Thresholds used for each model/condition were as follows: 5σ (model 0, 1, 2); 16σ (model 3; mitosis); 9σ (model 3; G_2); 12σ (model 3; mitosis with additional cohesin). Pearson correlations between experimental and simulated Capture-C directionality curves were as follows: -0.77 (model 0); 0.95 (model 1); 0.97 (model 2); 0.97 (model 3, mitosis); 0.69 (model 3, G_2; 0.96 in the region between -50 and 50 kbp from the middle of the CM); 0.98 (model 3, mitosis with additional cohesin).

To find the fraction of bipartite and monopartite structures, we analysed configurations from all simulations. The clustering algorithm in Stoddard[87] was used to find clusters of condensin bridges (or active condensin bridges in models with switching), with a threshold of 3σ for the 3D distance of any two bridges to be in the same cluster. Error bars were determined by assuming Poisson distributions.

In all simulations, the centre of the core centromere (CM beads) was modelled as an 11 kbp region in the middle of the simulated polymer. As epigenetic marks and histone binding is not solely determined by sequence, for visualisation we assumed CENP-A (orange in the snapshots) to bind an additional 10 kbp region on either side in the visualisation – in this way the CENP-A-covered region corresponds approximately to the core centromere size which is defined biologically (see shaded region in the experimental Capture-C plots). Importantly, this ~30 kbp boundary region (where the gradient in the Capture-C plot is the steepest) emerges from the model, it is not entered from an input (as the region in which bridge affinity to chromatin is altered in the force field is the internal 11 kbp region).

Simulated average ChIP-seq patterns (ChIP signals)

For each configuration in a simulation trajectory, and for each chromatin bead, condensin beads within a "cross-linking volume" (a sphere of size 4 σ) were added to the ChIP-seq signal. The overall signals were then averaged over simulations, and the average normalized.

Dynamic correlations

For each configuration, and each pair of chromatin beads (a particular pair is shown as examples in Figure S5), we computed the correlation between the displacement of the two beads over a fixed time window (corresponding to 1000 Brownian times).

QUANTIFICATION AND STATISTICAL ANALYSIS

Statistical analysis was performed with Prism 9 Software (Graphpad software). Representative results are displayed or all data were reported, as specified in individual figure legends. Data are presented as mean ± s.d. Specific statistical approaches were determined based on the distributions and parameters for each dataset. Information on statistical parameters, *p* values and number of independent experiments are specified in the figures and legends. All replicates showed similar results and a representative experiment was reported.

CellPress
OPEN ACCESS

Supplemental figures

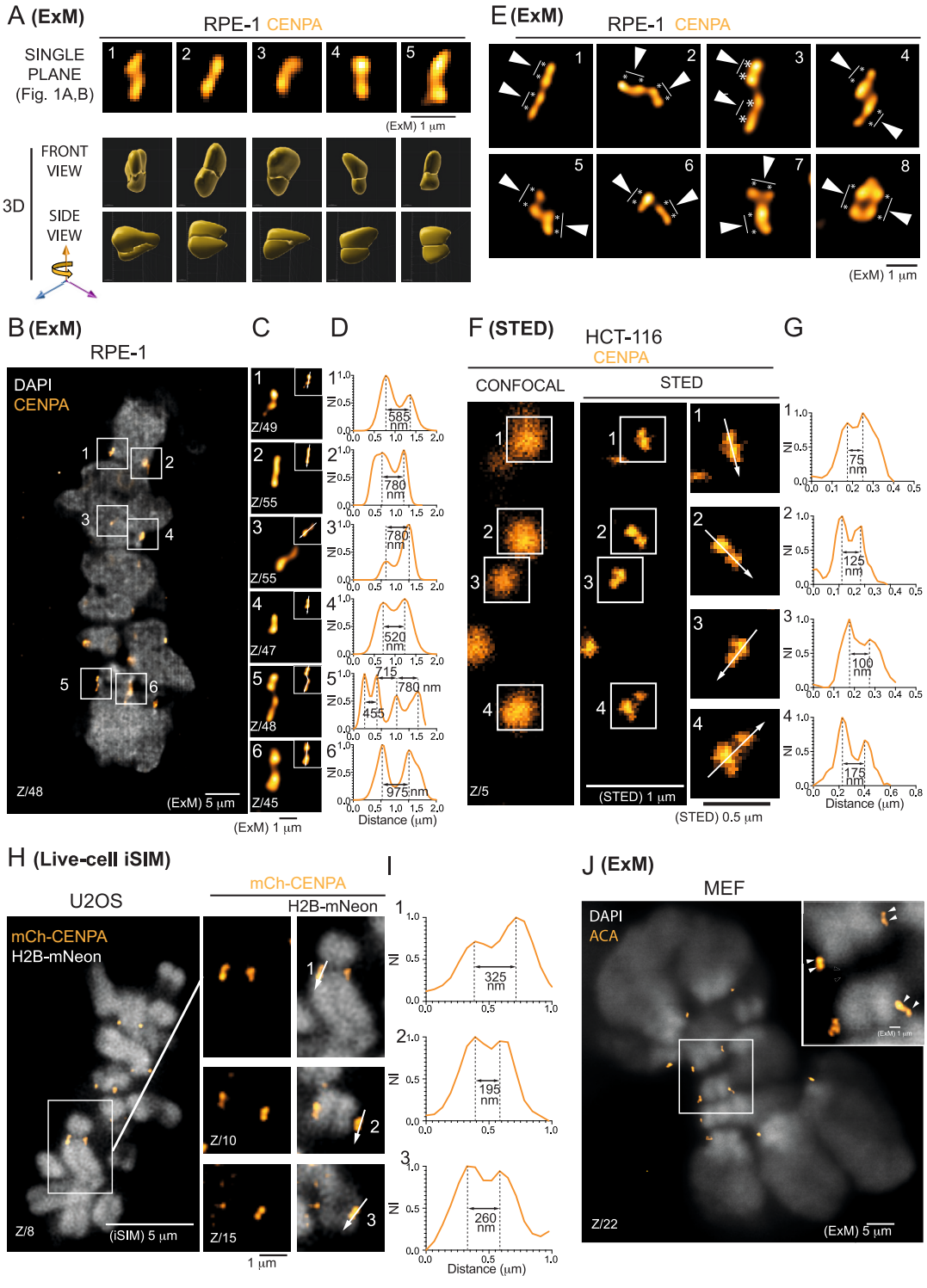

(legend on next page)

Figure S1. Subdomain organization of the regional centromere of vertebrates, related to Figure 1

(A) 3D reconstructions of the centromeres shown in Figures 1A and 1B.

(B–D) Representative ExM image of CENP-A in RPE-1 cells in metaphase (B). Blow-ups, centromeres enclosed in the boxes (C), and line intensity profiles across centromere subdomains (D). The distance between peaks is indicated.

(E) Examples of tetrapartite centromeres. Asterisks: small subdomains; arrowheads: main two subdomains.

(F and G) Immunostaining of CENP-A in HCT-116 cells imaged by confocal and STED microscopy. Numbered squares enclose the same centromeres in both conditions. Line intensity profiles across centromere subdomains (G). The distance between peaks is indicated.

(H and I) iSIM live-cell imaging (lateral resolution ~125 nm) of a U2OS cell expressing mCherry-CENP-A and H2B-mNeon (H). Blow-ups of the orange box and other regions are shown on the right. Line intensity profiles across centromere subdomains (I). The distance between peaks is indicated.

(J) Representative ExM image of a mouse embryonic fibroblast (MEF) immunostained with ACA (anti-centromere antibody). Arrowheads: ACA subdomains. The image belongs to the same cell shown in Figure 1H. Z specifies the plane of the z stack. NI, normalized intensity.

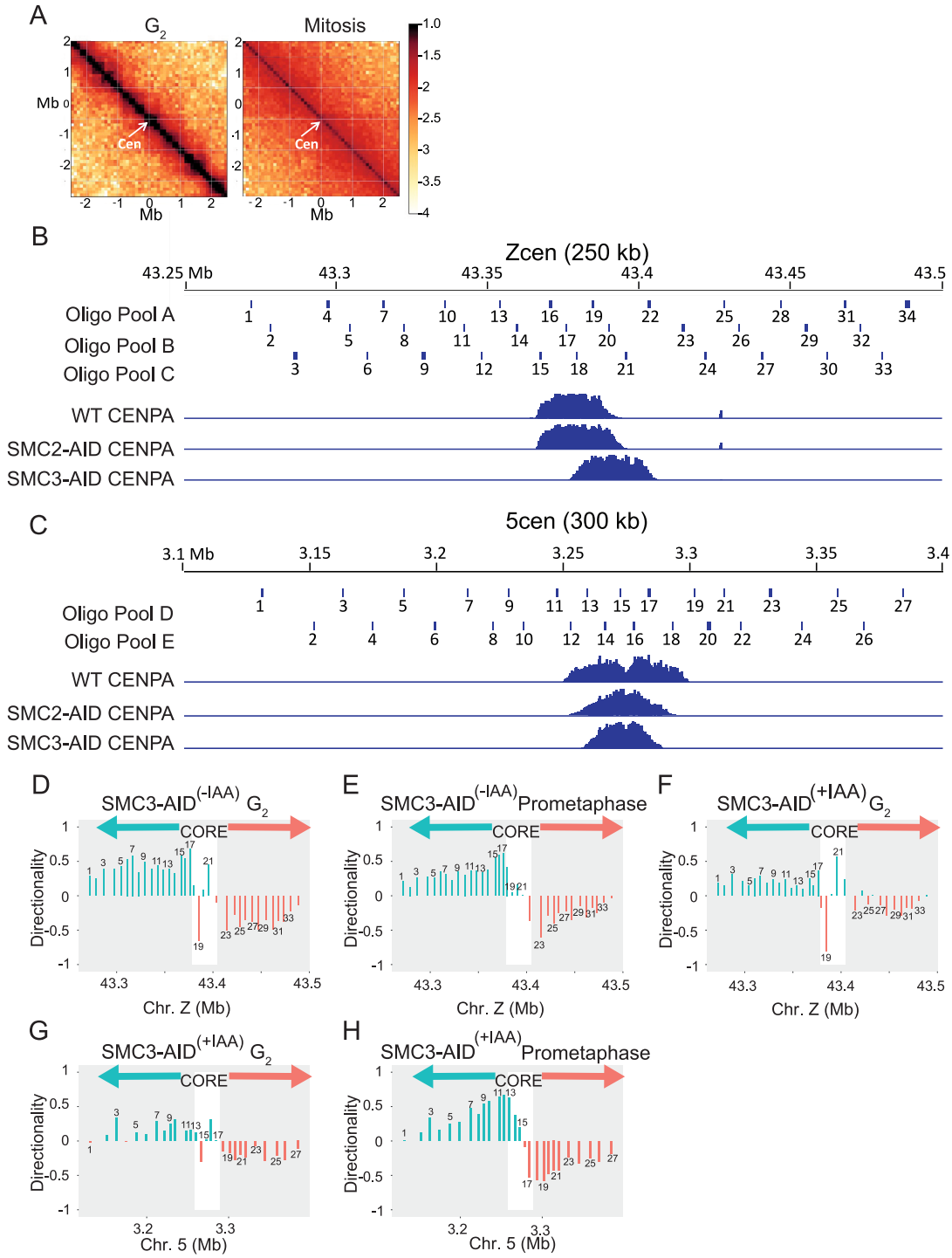

Figure S2. Bipartite mitotic centromeric chromatin organization of chicken Zcen and 5cen, related to Figures 2B–2E, 6J, 6K, S6F, and S6G

(A) Hi-C map of 2.5 MB region surrounding Zcen (arrow) in G_2 or in late prometaphase (T = 30 min after release from 1NMPP1). 100 kb resolution. Data are taken from Gibcus et al.[31]

(B and C) CENP-A ChIP-seq data to indicate the regions of the Z (B) and 5 (C) core centromeres of WT, SMC2-AID, and SMC3-AID CDK1^{as} subclone cell lines used for this study, and positions of capture oligos pairs (view points) surrounding (P1–P34) (B) and 5cen (P1–P27) (C). The core centromeric region is marked by a white box. Note: the core Zcen of SMC3-AID cells shifted toward the q arm by ~10 kb compared with WT and SMC2-AID cells due to centromere migration in this clone. Similarly, the 5cen positions varied among homologous chromosomes (WT) and sub-cell lines. It appeared that 5 cen positions in SMC3-AID clones are almost identical between two 5 chromosomes.

(legend continued on next page)

(D–H) Directionality of interactions at each view point of Zcen (D–F) and 5cen (G and H) in SMC3-AID G_2 and late prometaphase cells in the presence and absence of auxin, as indicated. Depletion of SMC3 does not affect to the directionality of interactions (see also Figure 6K). Core centromeric region (defined by the presence of CENP-A) is marked by the white box. Asymmetry in interaction is depicted by green upward bar (more interactions toward p arm) and by orange downward bar (more interactions toward q arm). x axis shows genomic DNA position in chromosome Z (D–F) and 5 (G and H). Value on the y axis is the natural log of the number of interactions toward the p arm divided by the number of interactions toward the q arm; only interactions with positions within a distance of 3–250 kbp of the viewpoint are included. The graphs represent the sum of two independent experiments.

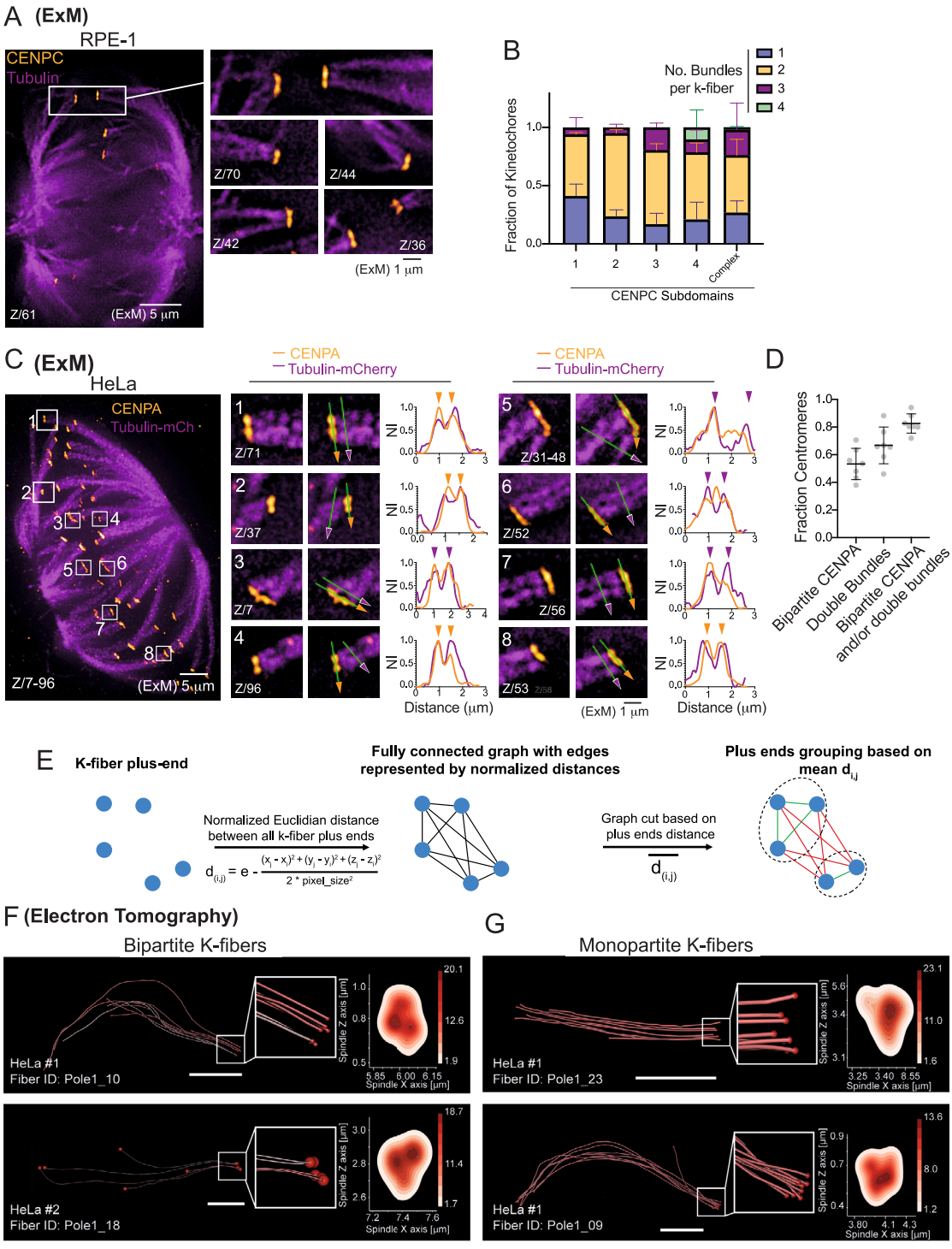

Figure S3. Kinetochore subdomains bind independent microtubule bundles, related to Figure 3

(A) ExM images (α-tubulin, CENP-C) in RPE-1 cells in metaphase. Blow-ups, kinetochores in the indicated planes. Cells were cold-treated before fixation.

(B) Fraction of centromeres in RPE-1 cells with the specified number of CENP-C subdomains that exhibit the indicated number of k-fiber bundles. Raw data are the same as that plotted in Figure 3C (mean ± SD of 2 independent experiments) (n = 11 cells, 474 centromeres).

(C) ExM image of a HeLa cell expressing mCherry-α-tubulin and immunostained for CENP-A. (Right) Blow-ups of the indicated centromeres and line scans across CENP-A subdomains and k-fibers. Double arrowheads: centromeres with two CENP-A subdomains (in orange) and/or double k-fibers (in magenta). Cells were cold-treated before fixation. NI, normalized intensity.

(legend continued on next page)

(D) Fraction of centromeres that show bipartite CENP-A signal and/or double k-fibers. Each dot represents one cell (mean ± SD of 1 experiment. *n* = 7 cells, 242 centromeres).

(E) Schematic illustration of quantification method used to model k-fiber splits based on the KMT plus-ends position. The plus ends of each k-fiber were extracted from electron tomography reconstructions published in Kiewisz et al.[34] Plus-ends positions were used to construct their fully connected graph representation, where the node (blue circle) represents each KMT plus end in the k-fiber and edges (black lines) are represented as normalized Euclidian distance. This allowed to represent complex kinetochore structures in a simplified two-dimensional (2D) view without any loss of information. The computed median distance between nodes was used as a threshold to define the graph cut area. The processed graph was then reversed to 3D coordinates from which the number of k-fiber splits at the kinetochore was calculated. See STAR Methods for details.

(F and G) Examples of electron-tomography 3D reconstruction showing k-fiber consisting of two microtubule bundles (indicated in different shades of red) (F) or a single bundle (G). The plus ends are indicated with dark red spheres. The kernel distance estimation plot of plus-end distribution along the xz axis is shown on the right. Z specifies the plane of the z stack. NI, normalized intensity.

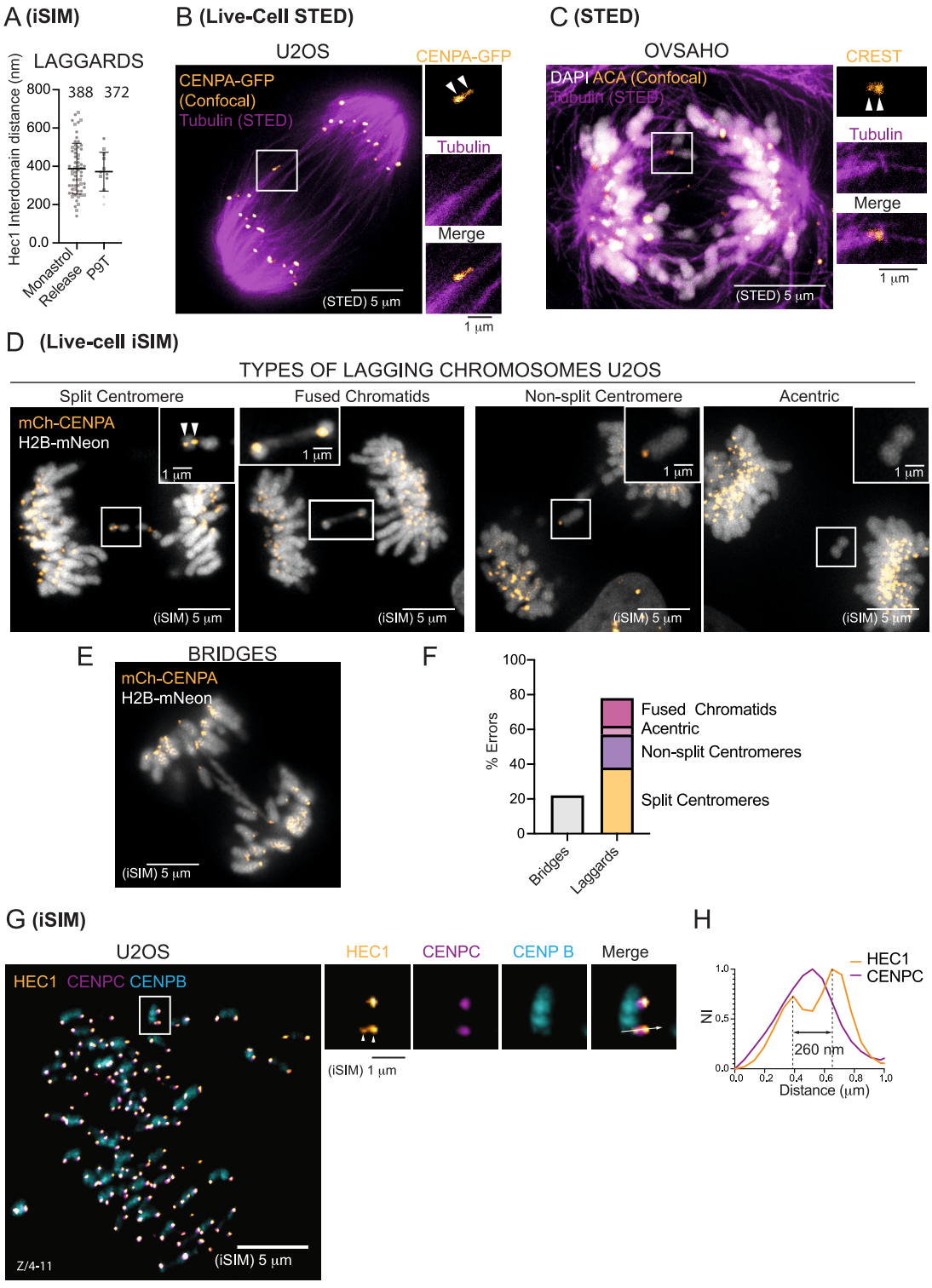

Figure S4. Merotelic attachments resulting from bioriented kinetochores in cancer cells, related to Figures 4 and 5

(A) Distance (iSIM) between bioriented HEC1 subdomains in lagging chromosomes of RPE-1 cells released from a monastrol arrest and in P9T cells (mean ± SD of pooled kinetochores from 3 independent experiments. Monastrol release, *n* = 62; P9T, *n* = 15 kinetochores). Dots, single kinetochores. See also Figures 4J–4L and 5H.

(B) Live-cell imaging of a lagging chromosome in a U2OS cell expressing CENP-A-GFP and stained with SiR-tubulin. Blow-ups of the boxed region are shown on the right. Note the two CENP-A (confocal) domains (arrowheads) attached to microtubules (STED) emanating from opposite spindle poles.

(legend continued on next page)

(C) Anaphase in an OVSAHO (high-grade serous ovarian) cell displaying a lagging chromosome with bi-oriented centromere subdomains (ACA, confocal) attached to microtubules (STED) from opposite spindle poles.
(D–F) iSIM live-cell imaging of the indicated types of chromosome segregation errors (D and E) in U2OS cells expressing mCherry-CENP-A and H2B-mNeon. The frequencies of each error type are quantified in (F). A total of 60 divisions were filmed in 3 independent experiments, of which 26 showed mitotic errors. Total number of observed errors = 37. All images are maximum projections in Z. Related to Figures 5B and 5C.
(G and H) iSIM image of an RPE-1 cell in metaphase after a monastrol release and stained with the indicated antibodies (G). Blow-up, a pair of sister kinetochores with one kinetochore displaying bioriented subdomains (arrowheads). Line intensity profiles across kinetochore subdomains are shown in (H), with the distance between peaks indicated. Z specifies the plane of the z stack. NI, normalized intensity.

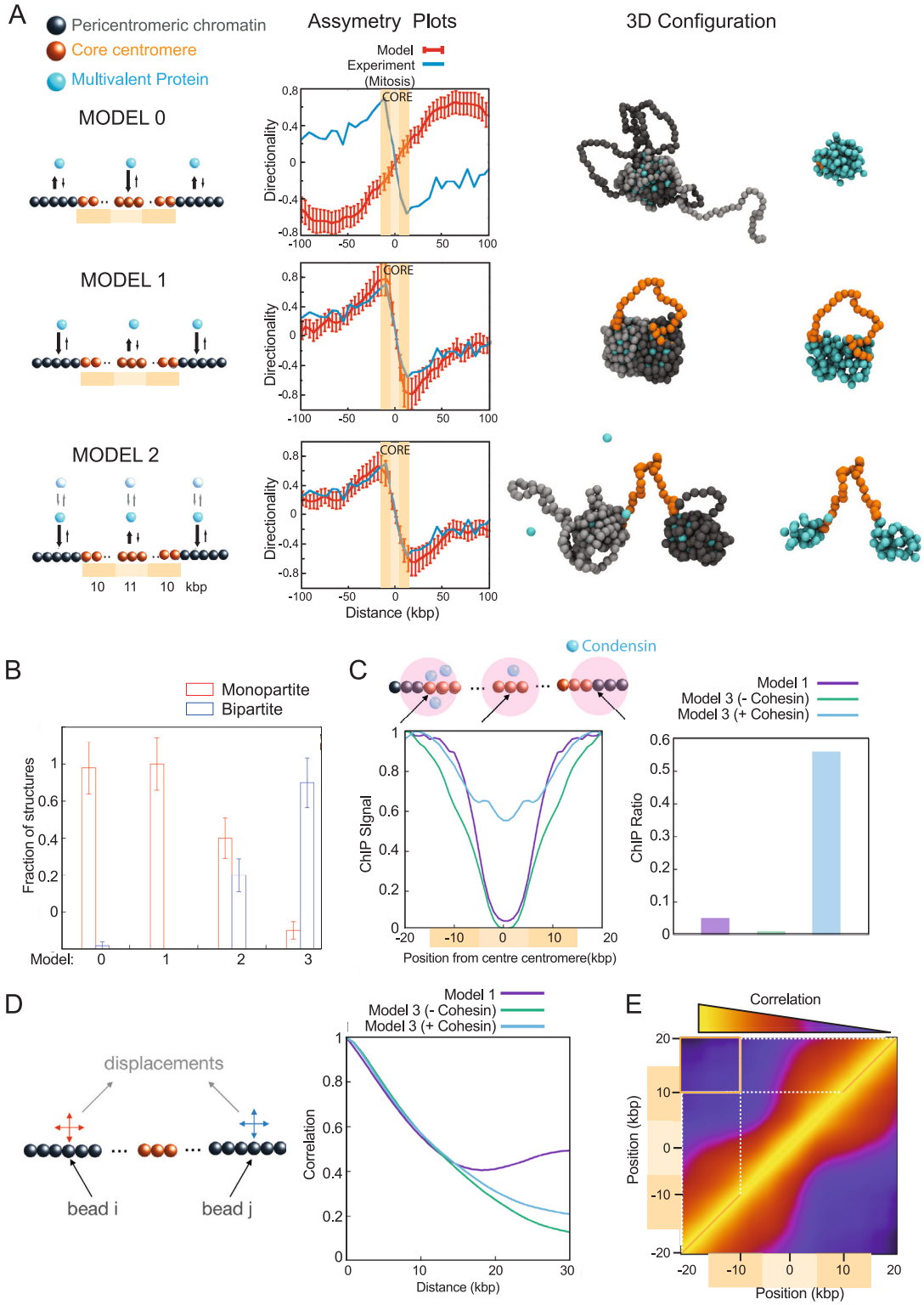

Figure S5. Polymer physics modeling of the centromere, related to Figures 6A–6C and 7A–7D

(A) Models 0, 1, and 2 of the centromere. All models consider one type of multivalent protein (MP), (or bridges, representing SMC proteins and other histone-binding proteins). The core centromere is represented with orange beads, while the pericentromere is represented with gray beads; each bead corresponds to 1 kb. The different models involve MP's varying affinities for the central region of the core centromere (11 kb, indicated with a lighter shade of orange) compared

(legend continued on next page)

with the pericentromere (in gray) and the borders of the core centromere (highlighted with darker shades of orange). Capture-C-like asymmetry plots and typical 3D configurations obtained in equilibrium are shown in the middle and right lines, respectively. In the 3D models, dark and light gray beads denote the two pericentromeric arms, orange beads denote the core centromere, and cyan beads denote the MP. In model 0, MP shows a higher affinity for the central region of the core centromere. This results in an "inverted" capture-C signal with respect to the mitotic one, and in a compact configuration that shows the core centromere buried in the structure. In model 1, MP binds more strongly to the pericentromere and core centromere borders than to the central region of the core centromere. This leads to a qualitatively correct capture-C signal, and to a switch in the core centromere location, which now is peripheral. In model 2, a nonequilibrium biochemical reaction of MP is included. This allows the switching of MP and leads to a bipartite organization in a significant portion of structures in the population (Figure S5B) while retaining the asymmetry in the contact pattern as observed by capture-C. See Figures 6A–6C and STAR Methods.

(B) Fraction of structures in the population of models 0, 1, 2, and 3 showing a monopartite or bipartite organization.

(C) The left graph illustrates the simulated average ChIP-seq patterns (ChIP signals), normalized to their maximum values, for model 1 and model 3 (with and without cohesin), within a 40 kbp region centered on the middle of the centromere. To construct the ChIP signals, condensin beads (light blue spheres) within a "cross-linking volume" (pink spheres) were added to the ChIP-seq signal and then normalized (see STAR Methods for details). The graph on the right represents the ratios between minimum and maximum values of the ChIP-seq signals (ChIP ratio) within the considered genomic range.

(D) Dynamic correlation over genomic distance (in kbp) for model 1 and model 3 (with and without cohesin). Plots were computed by averaging data for beads in a 40 kbp region centered on the centromere.

(E) Matrix showing the dynamic correlation in a 40 kbp region centered on the middle of the centromere, shown as a heatmap. The orange box denotes the region averaged to obtain data in Figure 7D. The matrix shown refers to model 3 with cohesin.

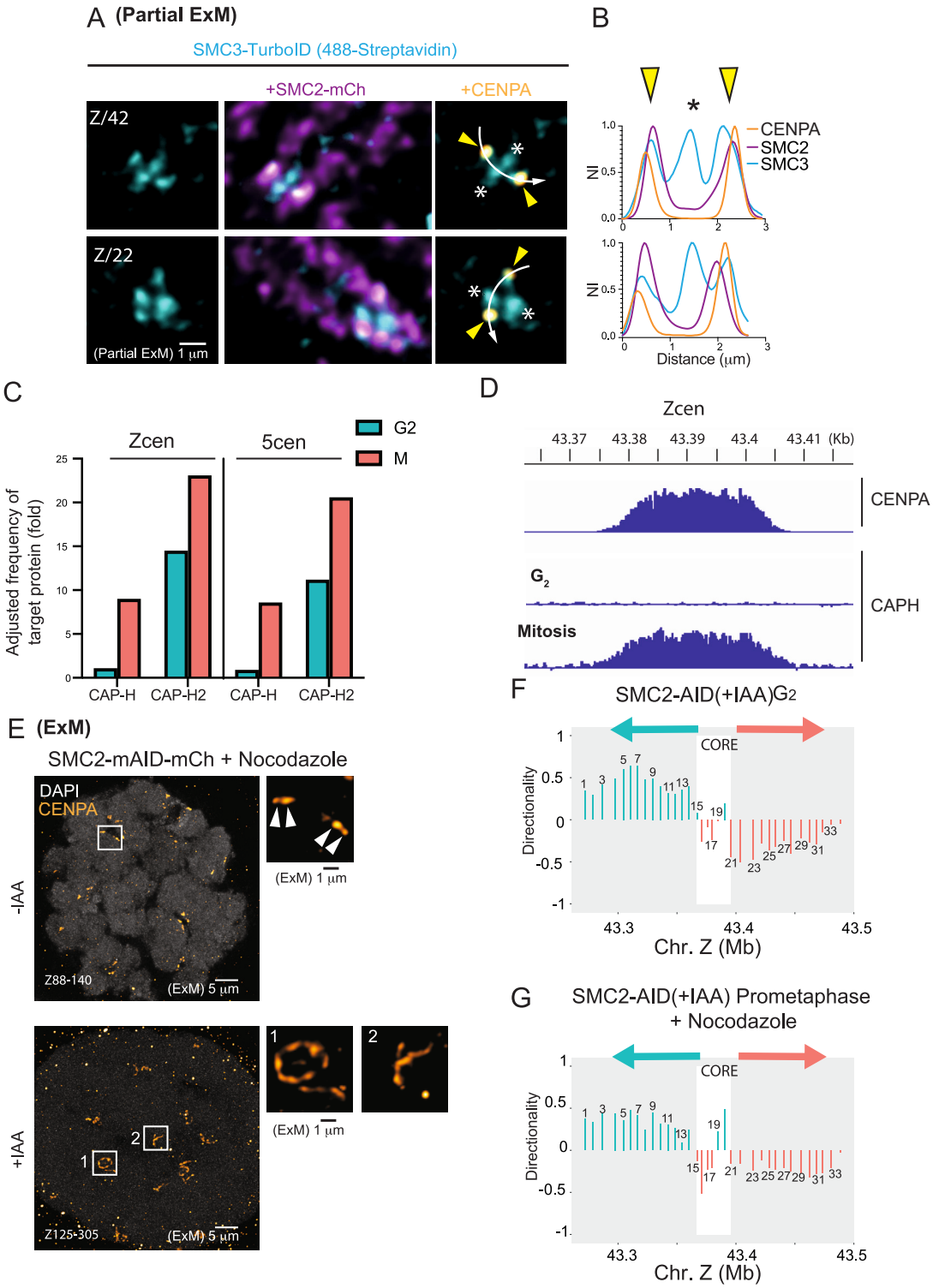

Figure S6. Centromeric localization and functions of condensin and cohesin, related to Figure 6

(A and B) Examples of chromosomes of the cell shown in Figure 6D (A). Line intensity profiles across sister centromeres (B). Yellow arrowheads: pool of cohesin proximal to the core centromere; asterisks: pool of cohesin at the inner centromere.

(C) Enrichment of the ChIP-seq (spike-in normalized) signal in the Z and 5 centromere of chicken cells relative to the chromosome arms for CAP-H (condensin I) and CAP-H2 (condensin II) during G_2 and mitosis.

(D) ChIP-seq of CENP-A and CAP-H in Z and 5 centromere of chicken G_2 and mitosis. The graph represents the sum of two independent experiments.

(legend continued on next page)

(E) ExM images of CENP-A in HCT-116$^{SMC2\text{-}mAID\text{-}mCherry}$ cells arrested in nocodazole (3.3 mM) and prepared in the absence or presence of auxin (IAA). (right) Blow-ups of the boxed areas. Arrowheads: CENP-A subdomains. See also Figure 6I.

(F and G) Directionality of interactions at each view point of Zcen in SMC2-AID G_2 (F) and SMC2-AID late prometaphase + nocodazole (G) treated with auxin. Asymmetry in interaction is depicted by green upward bar (more interactions toward p arm) and by orange downward bar (more interactions toward q arm). x axis shows genomic DNA position in Z chromosome. Value on the y axis is the natural log of the number of interactions toward the p arm divided by the number of interactions toward the q arm; only interactions with positions within a distance of 3–250 kbp of the viewpoint are included. The graphs represent the sum of two independent experiments. ChIP-seq data of CENP-A in these clones is shown in Figure S2B. Z specifies the plane of the z stack or high-intensity projections of the indicated planes. NI, normalized intensity.

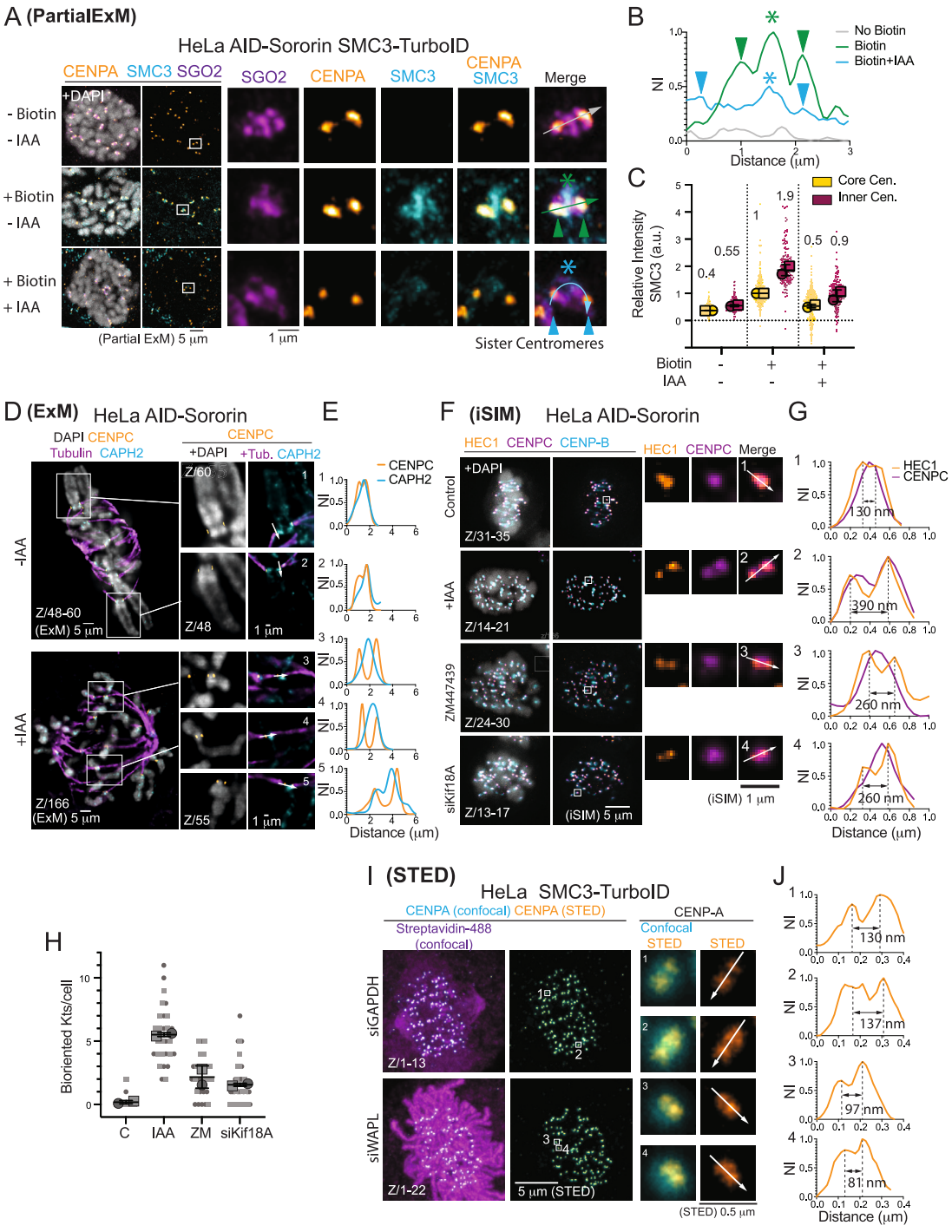

Figure S7. Cohesin stabilizes the bipartite centromere, related to Figure 7

(A–C) Partially expanded images of HeLa$^{Sororin\text{-}AID/SMC3\text{-}TurboID}$ cells stained as indicated (A). Cells were synchronized with thymidine, released in nocodazole, and treated with or without IAA, as specified. Biotin was added for 30 min before fixation. Biotinylated substrates were visualized with AF488-streptavidin. Blow-ups, sister kinetochore pairs for each condition. Line intensity profiles across sister centromeres (B). Arrowheads: pool of cohesin proximal to the core centromere; asterisks: pool of cohesin at the inner centromere. SMC3 relative levels at the core centromere (within the CENP-A signal) and the inner centromere (within the Sgo2 signal) are presented in (C). The data were normalized to the mean intensity of SMC3 within the core centromere of the positive control (mean ± SD of 2 independent experiments; Biotin^{-}IAA^{-} (core, n = 238; inner n = 172); Biotin^{+}IAA^{-} (core, n = 272, inner, n = 162) Biotin^{+}IAA^{+} (core, n = 343, inner, n = 199). Large dots, independent experiments; small dots, centromeres.

(legend continued on next page)

(D and E) ExM images of HeLa$^{Sororin\text{-}AID}$ cells prepared in the absence or presence of IAA and stained as indicated (D). Blow-ups of the boxed areas and other regions are shown on the right, and line intensity profiles across single kinetochores are depicted in (E). Related to Figure 7E.
(F–H) iSIM microscopy images of HeLa$^{Sororin\text{-}AID}$ cells stained with the indicated antibodies and treated as indicated. Cells were released from an RO-3306 arrest and fixed 1 h later. The control was additionally treated with siGAPDH. Line intensity profiles across subdomains are shown in (G), with the distance between peaks indicated. Quantifications of the number of bioriented kinetochores per cell under different conditions are depicted in (H). Mean ± SD of 2 independent experiments; control, $n = 27$; IAA, $n = 28$, ZM, $n = 37$, siKif18A $n = 27$. Large dots, independent experiments. Small dots, individual cells. Related to Figures 7J–7L.
(I and J) STED images of CENP-A in HeLa$^{AID\text{-}Sororin/SMC3\text{-}TurboID}$ treated with the indicated siRNAs. Cells were synchronized with RO-3306, and biotin was added for 30 min before fixation. Biotinylated substrates were visualized with AF488-streptavidin with confocal resolution. Line intensity profiles across centromere subdomains (J), with the distance between peaks indicated. Related to Figure 7N.